UNIVERSITY OF BIRMINGHAM
University of Birmingham Research at Birmingham

A study of the influence of separation bubbles around a generic freight train on pressure waves inside tunnels using 1D and 3D numerical methods

Liu, Zhen; Soper, David; Hemida, Hassan; Chen, Boyang

DOI:
10.1016/j.jweia.2023.105461

License:
Creative Commons: Attribution (CC BY)

Document Version
Publisher's PDF, also known as Version of record

Citation for published version (Harvard):
Liu, Z, Soper, D, Hemida, H & Chen, B 2023, 'A study of the influence of separation bubbles around a generic freight train on pressure waves inside tunnels using 1D and 3D numerical methods', *Journal of Wind Engineering and Industrial Aerodynamics*, vol. 240, 105461. https://doi.org/10.1016/j.jweia.2023.105461

Link to publication on Research at Birmingham portal

General rights
Unless a licence is specified above, all rights (including copyright and moral rights) in this document are retained by the authors and/or the copyright holders. The express permission of the copyright holder must be obtained for any use of this material other than for purposes permitted by law.

•Users may freely distribute the URL that is used to identify this publication.
•Users may download and/or print one copy of the publication from the University of Birmingham research portal for the purpose of private study or non-commercial research.
•User may use extracts from the document in line with the concept of 'fair dealing' under the Copyright, Designs and Patents Act 1988 (?)
•Users may not further distribute the material nor use it for the purposes of commercial gain.

Where a licence is displayed above, please note the terms and conditions of the licence govern your use of this document.

When citing, please reference the published version.

Take down policy
While the University of Birmingham exercises care and attention in making items available there are rare occasions when an item has been uploaded in error or has been deemed to be commercially or otherwise sensitive.

If you believe that this is the case for this document, please contact UBIRA@lists.bham.ac.uk providing details and we will remove access to the work immediately and investigate.

Download date: 28. Apr. 2024

Journal of Wind Engineering & Industrial Aerodynamics 240 (2023) 105461

Contents lists available at ScienceDirect

Journal of Wind Engineering & Industrial Aerodynamics

journal homepage: www.elsevier.com/locate/jweia

A study of the influence of separation bubbles around a generic freight train on pressure waves inside tunnels using 1D and 3D numerical methods

Zhen Liu *, David Soper, Hassan Hemida, Boyang Chen

School of Engineering, University of Birmingham, Birmingham, B15 2TT, UK

ARTICLE INFO

Keywords:
Freight train
Computational Fluid Dynamics
One-dimensional numerical method
Train/tunnel aerodynamics
Large Eddy Simulation

ABSTRACT

Due to the increased effective blockage area caused by the bluff nature of a freight train, traditional one-dimensional (1D) numerical modelling techniques struggle to predict the initial pressure wave formation for these train types. This paper presents, for the first time, a detailed study of this phenomenon for typical freight train locomotives, and a redeveloped 1D code capable of solving for bluff freight vehicles. Firstly, a 1D numerical model for tunnel pressure development is written and validated with previous research. Then, 3D simulations using computational fluid dynamics (CFD) have been carried out to model a freight train entering into a tunnel, with a view to characterising the key regions of flow separation. According to this, the 1D code is redeveloped to simulate the changing effective blockage area of the freight train, caused by flow separation at the blunted train head. A separation bubble model is built to calculate the effective blockage area. Results show that the error between the results obtained from the modified 1D model and the experiment is significantly reduced in relation to traditional 1D numerical models. To provide further functionality through the ability to apply the model to various types of freight train locomotives, a parameterisation study is conducted to obtain the relationship between the vehicle shape (bluntness) and new input parameters for the separation bubble model. Finally, the separation bubble model and parameterisation equation is tested to validate its applicability, with results indicating good agreement for a range of train designs.

1. Introduction

The UK government aims to double the volume of rail freight cargo on the UK rail network by 2030 (DfT, 2007). Opportunities highlighted to achieve this aim include the introduction of dedicated high-speed freight. However, increasing train speeds can cause a series of aerodynamic issues, including slipstream effects for platform passengers and trackside workers, as well as tunnel pressure magnitudes, which act as barriers to the implementation of higher freight train speeds. For example, the amplitude of pressure change increases approximately proportional to the square of train speed (Li et al., 2011). Furthermore, aerodynamic problems are more obvious when the train is running in a confined space, such as a tunnel (Liu et al., 2021). Though numerous studies have been conducted to consider the aerodynamics of trains in tunnels, the majority have purely focused on passenger trains, due to the speed at which these vehicles travel. Although traditionally travelling at much lower speeds, there are still aerodynamic issues that need to be considered for freight trains passing through a tunnel, due to the 'bluff' nature of these vehicles.

As a train enters into a tunnel, the nose of the train pushes the air ahead of it, generating a compression wave that propagates to the tunnel exit with the speed of sound (Howe et al., 2003; Liu et al., 2010). This compression wave leads to a sudden pressure rise where it passes. This can lead to safety concerns in the tunnel environment, especially in relation to aural discomfort for passengers/workers in the locality. With the improvement of computational ability, massive computational fluid dynamics (CFD) simulations can be undertaken using commercial software to achieve a better knowledge and characterisation of the flow field when trains pass through tunnels (Liu et al., 2021; Howe et al., 2003; Ogawa and Fujii, 1997; Cross et al., 2015). The simulation of a moving train is however very computationally expensive and time-consuming. Munoz-Paniagua et al. (2014) conducted optimisation of the train nose shape to minimise the maximum pressure gradient and drag during tunnel entry. This was achieved using a surrogate-based optimiser, which employed a surrogate model to substitute CFD solver calls, thereby reducing computational costs. Since the length of the tunnel is much larger than the diameter of the tunnel section, the pressure fluctuation over a certain cross-section of the tunnel can be neglected compared to its variation with time (Woods and Pope, 1981). Subsequently many researchers have developed one-dimensional (1D) numerical models to calculate a quick, less computationally intensive

* Corresponding author.
E-mail address: 15581666545@163.com (Z. Liu).

https://doi.org/10.1016/j.jweia.2023.105461
Received 8 December 2022; Received in revised form 4 April 2023; Accepted 20 May 2023
Available online 12 June 2023
0167-6105/Crown Copyright © 2023 Published by Elsevier Ltd. This is an open access article under the CC BY license (http://creativecommons.org/licenses/by/4.0/).

solution to the pressure variation in tunnels (Vardy and Reinke, 1999; William-Louis and Gregoire, 2002; Fox and Henson, 1971). Compared to 3D CFD simulations, which can take days/months to simulate a train passing through a tunnel, it may only take seconds or minutes for a 1D code to obtain an accurate result of the pressure variations. Furthermore, it has also been shown to provide reasonable results for project demands, especially having the advantage of being able to model train crossing and extra-long tunnels with constant cross-section area (Raghunathan et al., 2002). This is therefore an invaluable technique in an industry setting for testing many different scenarios in the initial design stage for new trains and/or tunnels.

Freight trains however typically look very different to passenger trains, for which these 1D numerical techniques and studies have been traditionally designed/undertaken for. Due to the blunted nose shape of freight trains and discontinuities along the train length, these vehicles generate a unique characteristic pressure wave pattern, that is different from that of a passenger train as they pass through a tunnel. The separation bubble induced by the blunted head will increase the effective blockage ratio, and further notably increase the magnitude of the initial pressure rise (Iliadis et al., 2019). It also has a lasting impact on the subsequent pressure changes as the pressure wave propagates inside the tunnel. These phenomena are not able to be well predicted through traditional 1D methods, since the influence of the train nose shape on the compression wave is represented only by pressure loss and cross-sectional area. Furthermore, for passenger studies the cross-sectional area of the train body is considered a constant value in the traditional method, which is often not the case for freight trains with a range of wagon types and/or container loading patterns. As a result, the pressure change caused by the separation bubble at the bluff train head is not able to be accurately predicted in traditional 1D methods.

Flow around a freight train is similar to bluff body flow, on which research is mainly focused on basic fundamental investigations in low Re number (Lim et al., 2009; Gao and Chow, 2005; Chen and Shao, 2013; Paik et al., 2009). As air flows over an “elongated” bluff body, the flow will separate at the leading edge, followed by reattachment along the body. A wide range of experiments have been carried out to study the leading edge flow separation (Taylor et al., 2011), including studies extended towards rail for container type freight train configurations in the open air (Soper et al., 2014; Flynn et al., 2014; Kocoń and Flaga, 2021; Li et al., 2017; Giappino et al., 2018). Results indicate that the leading separation angle, which also acts as an indicator to the bluffness of a geometry, plays an important role in the formation of the leading edge separation bubble (Taylor et al., 2011). Li et al. (2017, 2015) investigate the flow topology of a double-stacked container wagon subject to different combinations of front and rear gap sizes. Results indicate that the leading edge separation zone at each container is similar to flow over a surface-mounted cube. Furthermore, the pressure distribution across the train surface and the separation reattachment length are measured, which have been subsequently used by modellers for validation purposes (Maleki et al., 2017, 2019). The leading edge flow separation at a freight train nose has also been analysed through the use of vertical and lateral velocity measurements in physical modelling experiments (Soper, 2016; Soper et al., 2014). A characteristic positive, then negative velocity peak is observed at the freight train nose and container leading faces, indicating a flow reversal zone caused by separation.

With the development of computing capability, computational methods have been developed and implemented to explore the flow around a bluff-body. Large Eddy Simulation (LES) techniques have been shown to be very suitable for addressing this type of flow and widely implemented to study the flow structures around basic models (e.g. cubes, square cylinders Rocchio et al., 2020; Lim et al., 2009; Richards and Norris, 2015; Krajnovic and Davidson, 2002 buildings Liu et al., 2020) and generic bluff ground vehicles (e.g. bus, Ahmed body, etc. Keogh et al., 2016; Krajnović and Davidson, 2005a). This is not only due to the flow field around the bluff body being dominated by large-scale vortices, generated as the air flows over sharp edges, but also due to the Reynolds number being very small within this type of separation region, resulting in a relatively low mesh resolution requirement (Krajnović, 2009; Krajnović and Davidson, 2005a). Further investigations on flow patterns and force coefficients for freight trains with a bluff train head and differing wagon shapes have also been conducted using the LES technique (Östh and Krajnović, 2014; Hemida and Baker, 2010; Maleki et al., 2019, 2017; Khayrullina et al., 2015), IDDES (Huo et al., 2022; Liang et al., 2023) and RANS (Kedare et al., 2015). It is found that complex flow structures and flow separations, which are different from the flow development around passenger trains, are formed around freight wagons (Hemida and Baker, 2010). Separation bubbles are observed on the roof and side of the train, which is similar to the flow characteristics that occur for a cube or generic bluff-body (Östh and Krajnović, 2014). The separation bubble on the roof was found to be around $1.75W$ in length and $0.35W$ in height (where W is the width of the train) for the single wagon with a Reynolds number of 10^5. Maleki et al. (2017) assessed the capabilities of RANS, ELES and SAS on predicting the flow characteristics (pressure and velocity variation, aerodynamic drag) around a freight wagon. The results obtained from ELES and SAS simulations are validated and analysed quantitatively, with both models indicating good agreement with experimental techniques. However, whilst the steady RANS model is capable of predicting the trend in pressure, it performed badly for individual drag prediction.

Based on current research, it can be concluded that while traditional 1D methods offer a significant advantage in rapidly predicting pressure variations as a train passes through a tunnel, current methods are incapable of accurately predicting the pressure increase caused by bluff freight trains, due to the non-aerodynamic shape. This innovative paper has developed a modified 1D flow methodology that is capable of accurately predicting the pressure wave generated by a wide range of freight trains passing through a tunnel. Firstly, the numerical methods and geometries used in this paper are introduced in tail in Section 2. Modifications were made to the boundary conditions at the train head and governing equations, to account for the changes in effective cross-sectional area induced by flow separation at the bluff train head. A separation bubble model is proposed in Section 3.1 and introduced into the 1D numerical methodology to describe the shape of the separation region. To support the development of this approach for a wide range of freight vehicle types, a parameterisation study was carried out with consideration of different leading edge separation angles and tunnel cross-sectional areas in Sections 3.2 and 3.3. The proposed model and parameterisation equations are validated using further independent simulations for a Class 70 locomotive in Section 3.5. The results of this paper offer important insights for the initial design of freight trains and tunnels.

2. Numerical simulation

2.1. Geometry

A 1/25 scale Class 66 freight locomotive connected to simplified FEA-B wagons loaded with ISO containers is used in this study, as shown in Fig. 1. The features and shape of the nose and underbody are kept consistent with the physical model used in the experiments by Iliadis et al. (2019); data from which are used to validate findings in this study. Minor simplifications have been made to the bogies to facilitate the division of structured mesh and enable a higher mesh quality. However, the length and height of the bogies and diameter of the wheels are the same as those used in the experiment, to keep the blockage area unchanged, as it is believed to be one of the main parameters that influences pressure waves. The locomotive has a scale height of $H = 0.157$ m and width of $W = 0.107$ m. These dimensions will be used in the parameterisation study to non-dimensionalise the

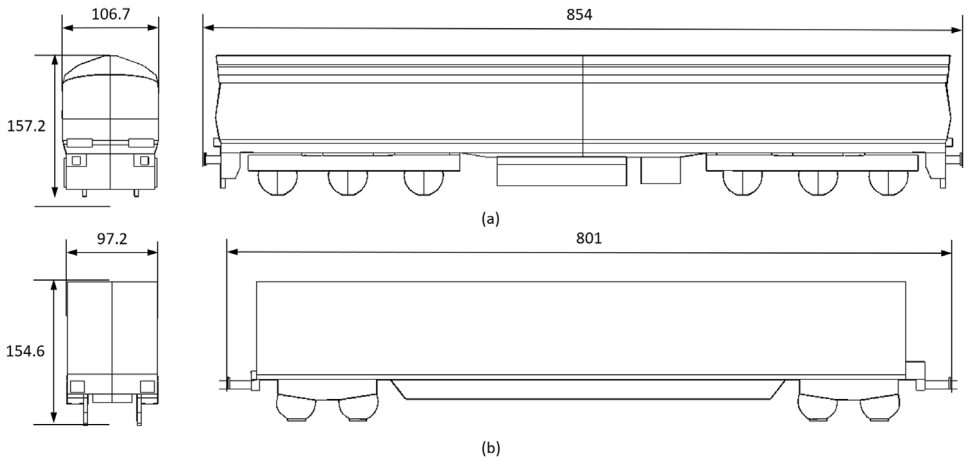

Fig. 1. Dimensions of the freight train CAD model (a) Class 66 locomotive (b) FEA-B wagons without containers. All dimensions in the reduced 1/25th scale and given in mm.

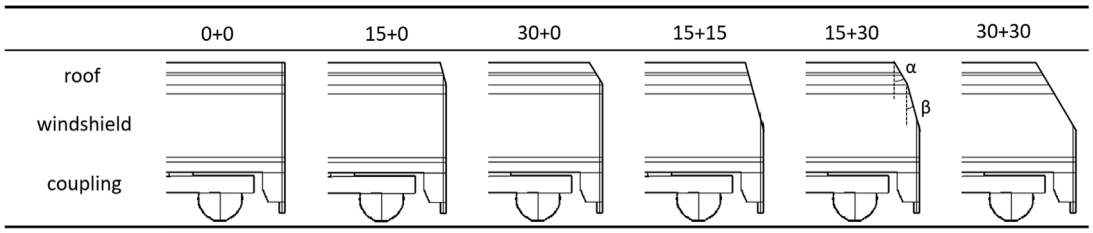

Fig. 2. Different head shapes of the generic freight locomotive utilised in the parameterisation study.

separation bubble size. Further details for the Class 66 and wagon dimensions are given in Fig. 1 and described (Flynn et al., 2014).

For the parameterisation study of nose bluntness, the Class 66 locomotive is simplified to a generic freight locomotive shape, and divided into three distinct regions (roof, windshield and coupling). The bluffness can therefore be controlled by changing α and β (as shown in Fig. 2), where α and β are the angles between the windward side and the vertical line of the roof and windshield region respectively. By considering a wide range of European locomotive types and shapes, it can be observed that, for all locomotive types, both angles fall in the range of [0,30]. Therefore, six combinations of angles ($\alpha + \beta$) are used to conduct the parameterisation study; which are $0+0$, $15+0$, $15+15$, $30+0$, $30+15$, $30+30$ respectively as shown in Fig. 2.

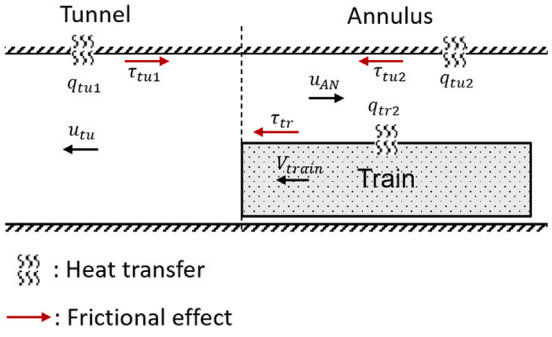

Fig. 3. Diagram of the flow model.

2.2. 1D code

2.2.1. Numerical method

A 1D code is written based on an unsteady, compressible, non-homentropic flow model. This model is validated by comparison to previous research with full-scale experiment data, suggesting that the numerical method can predict temperature, velocity, and pressure variations accurately, and therefore be commonly adopted by researchers and industry (Woods and Pope, 1981; Vardy, 1976; Mei, 2013). In this model, the heat transfer and friction effect between air and train/tunnel walls are considered, with the air inside the tunnel modelled as an ideal gas. The continuity, momentum and energy equations are given as Eqs. (1)–(3) and the diagram of this flow model is given in Fig. 3 for further illustration.

$$\frac{\partial \rho}{\partial t} + u\frac{\partial \rho}{\partial x} + \rho\frac{\partial u}{\partial x} = 0 \tag{1}$$

$$\frac{\partial u}{\partial t} + u\frac{\partial u}{\partial x} + \frac{1}{\rho}\frac{\partial p}{\partial x} + \boldsymbol{g} = 0 \tag{2}$$

$$\left(\frac{\partial p}{\partial t} + u\frac{\partial p}{\partial x}\right) - a^2\left(\frac{\partial \rho}{\partial t} + u\frac{\partial \rho}{\partial x}\right) = (\boldsymbol{q} - \boldsymbol{w} + u\boldsymbol{g})\rho(\kappa - 1) \tag{3}$$

where E is cross-sectional area, a is the local speed of sound, $\boldsymbol{g}$ is the friction term, $\boldsymbol{q}$ is the heat-transfer term and $\boldsymbol{w}$ the work-transfer term. The frictional force in this code is calculated considering the steady wall shear stress $\tau \approx \frac{1}{2} f \rho u|u|$. Thus giving the equation to calculate the fictional force acting on per unit mass of air in empty tunnel,

$$\boldsymbol{g}_{TU} = \frac{S_{TU}}{2E_{TU}} f_{TU} u|u| \tag{4}$$

For the air in the annulus between a train and tunnel, fictional force is the sum of the force acting on the tunnel and train surface (τ_{tu2} and τ_{tr} respectively, as shown in Fig. 3).

$$\boldsymbol{g}_{AN} = \frac{S_{TU}}{2F_{AN}} f_{TU} u|u| + \frac{S_{TR}}{2F_{AN}} f_{TR}(u - V)|u - V| \tag{5}$$

in which V is the speed of the train. The heat convection between the air and tunnel surface, air and train surface is considered in this flow model, as it is seen to contribute the most to the heat transfer term. According to the Newton's law of cooling, heat convection is proportional to the temperature difference between air and wall surface,

$$Q = hA\left(T_w - T_\infty\right) = hSL\left(T_w - T_\infty\right) \tag{6}$$

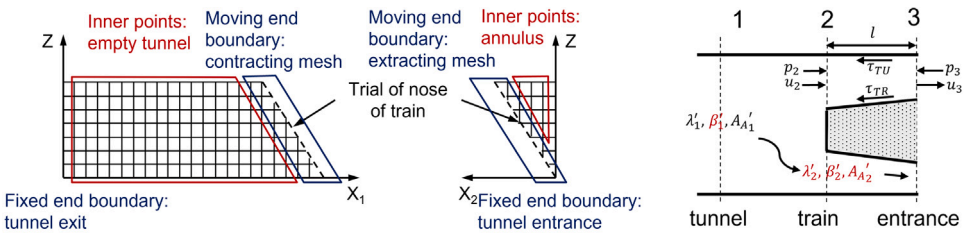

Fig. 4. Diagram of the mesh division (a) Mesh system for the first phase (b) Boundary condition when train nose enters a tunnel (variables marked in red are the unknowns that need to be solved).

in which T_w and T_∞ are wall and air temperature separately. h is heat convection coefficient $h = \frac{1}{2}\rho f\,|u'|\,C_p$, in which C_p is the specific constant of air and u' is the air velocity relative to the wall. Thus leading to the heat transfer term in an empty tunnel and annulus between the tunnel and train,

$$q_{TU} = \frac{S_{TU}}{2E_{TU}}\frac{\kappa R}{\kappa-1} f_{TU}|u|\left(T_{TU}-T\right) \tag{7}$$

$$q_{AN} = q_{TU} + q_{TR} = \frac{S_{TU}}{2E_{AN}}\frac{\kappa R}{\kappa-1} f_{TU}|u|\left(T_{TU}-T\right) + \frac{S_{TR}}{2E_{AN}}\frac{\kappa R}{\kappa-1} f_{TR}|u-V|\left(T_{TR}-T\right) \tag{8}$$

The work transfer term refers to the work on the control element done by the moving wall surface. Since there is no relative motion between the tunnel wall surface and control element in the ground coordinate system, the work transfer term in empty tunnel is,

$$w_{TU} = 0 \tag{9}$$

For the annulus between train and tunnel, the work on the control element done by the frictional force of the moving train surface per unit time per unit mass is,

$$w_{AN} = \frac{S_{TR}}{2E_{AN}} f_{TR} V(u-V)|u-V| \tag{10}$$

Hence altogether this provides the full expression of terms in continuity, momentum and energy equation for the 1D flow model. The well-known mathematical method to solve the set of quasi-linear hyperbolic partial differential equations is the MOC (method of characteristics). Details on this numerical method are introduced in Appendix.

2.2.2. Mesh system and boundary conditions

To simulate the moving train in the 1D code, the mesh is divided into several separated ducts by train ends and tunnel portals, which are regarded as non-continuous boundaries in the 1D code. The length of these ducts changes as the train passes through the tunnel. Each duct representing the train and tunnel is divided into a mesh size of 0.005 m, and the left-hand end is fixed while the right-hand end is movable. This idea was first introduced in Woods and Gawthorpe (1972) and has been adopted in most programmes to date (William-Louis and Gregoire, 2002; Mei, 2013; Woods and Pope, 1981). The whole process of a train entering the tunnel is composed of three phases, due to the different expanding and contracting mesh in each phase. Fig. 4(a) shows the first phase, which is the period of the train entering tunnel. It contains two mesh systems: duct1 is an empty tunnel that contracts in length and duct2 is an annulus that expands in length. Both with a moving end that is the nose of the train head. The fixed left-hand ends are the tunnel exit and entrance. All inner points in each duct are calculated using the method introduced in Section 2.2.1. The boundaries at the ends of each mesh (tunnel portals and train head/tail) need to be calculated separately by flow equations in conjunction with the characteristic equation (Woods and Pope, 1981).

Due to the complexity caused by considering the area change of the separation bubble at the train nose, the equations to solve the boundary condition of the train nose entering a tunnel are modified and illustrated as Eqs. (11) to (14),

$$\left(\lambda_1'+\beta_1'\right)^2 - \left(\lambda_2'+\beta_2'\right)^2 + \frac{2}{\kappa-1}\left[\left(\lambda_1'-\beta_1'\right)^2 - \left(\lambda_2'-\beta_2'\right)^2\right] = 0 \tag{11}$$

$$\left(\lambda_1'-\beta_1'\right)^2\left(\lambda_1'+\beta_1'\right)^{\frac{2}{\kappa-1}}\left(\frac{A_{A_2}}{A_{A_1}}\right)^{\frac{2\kappa}{\kappa-1}} - \frac{E_2}{E_1}\left(\lambda_2'-\beta_2'\right)\left(\lambda_2'+\beta_2'\right)^{\frac{2}{\kappa-1}} = 0 \tag{12}$$

$$\frac{A_{A_2}}{A_{A_1}} = \left(1 + \frac{\frac{2\kappa}{(\kappa-1)^2}\left(\frac{\lambda_2'-\beta_2'}{\lambda_2'+\beta_2'}\right)^2\zeta_N}{\left[1+\frac{2}{\kappa-1}\left(\frac{\lambda_2'-\beta_2'}{\lambda_2'+\beta_2'}\right)^2\right]^{\frac{\kappa}{\kappa-1}}}\right)^{\left(\frac{\kappa-1}{2\kappa}\right)} \tag{13}$$

For train heads entering tunnel:

$$\left(\frac{\lambda_2'+\beta_2'}{2A_{A_2}}\right)^{\frac{2\kappa}{\kappa-1}} = \frac{1}{p_R}\left\{\frac{p_3}{\phi} + \rho_3 a_R^2(\phi-1)\left(\frac{\lambda_2'-\beta_2'}{\kappa-1}+\frac{V}{a_R}\right)^2 + \frac{\rho_3 l a_R^2}{2E_2}\left[\frac{f_{TU}S_{TU}}{4}\left[(\phi+1)\left(\frac{\lambda_2'-\beta_2'}{\kappa-1}+\frac{V}{a_R}\right)\right]^2 + \frac{f_{TR}S_{TR}}{4}\left[(\phi+1)\left(\frac{\lambda_2'-\beta_2'}{\kappa-1}\right)\right]^2\right]\right\} \tag{14}$$

For train head inside tunnel:

$$\beta_2' = \beta_{2S}' + C_1' A_{A_2} + \delta C_f + \delta C_h + \delta C_a \tag{15}$$

where λ', β', and A_A are the Riemann variables relative to the train, κ is an air constant, E and S represent the area and perimeter respectively. Fig. 4(b) is the diagram of the boundary condition for the train nose entering the tunnel, in which λ_1' and A_{A_1} are known variables that can be calculated from the previous time step. $\beta_1', \lambda_2', \beta_2'$, and A_{A2} are the four unknown variables that need to be calculated by flow Eqs. (11)~(14). These equations are solved using the Newton–Raphson method in the code with a residual less than e^{-6}. Eqs. (11)~(12) are deducted from the continuity equation and momentum equation of the flow from 1 to 2 in Fig. 4(b). Eq. (13) is deducted from the thermodynamic relationship of the flow between 1 and 2 and the definition of pressure loss coefficient $\zeta_N = \frac{P_{02}-P_{01}}{0.5\rho_2 u_2'}$. Eq. (14) is deducted from the continuity and momentum equation of the flow from 2 to 3, as shown in Eqs. (16)~(17), $\phi = \frac{E_2}{E_3}$. Here it is assumed that the distance l is sufficiently small such that the density is uniform over the element $(\rho_2 = \rho_3)$.

$$\rho_2 E_2 u_2 = \rho_3 E_3 u_3 \tag{16}$$

$$p_2 E_2 + \rho_2 E_2 u_2^2 = p_3 E_3 + \rho_3 E_3 u_3^2 + 0.5\rho_3 l\left[f_{tu}\bar{u}^2 S_{tu} + f_{tr}\left(\bar{u}-V_{tr}\right)^2 S_{tr}\right] \tag{17}$$

Table 1
Freight train parameters used in the traditional 1D code (before 1:25 reduced scale).

Name	Length	Area	Perimeter	Friction coefficient	Head loss	Tail loss	Velocity
Loco66	182 m	10.5 m^2	9.82 m	0.005	0.1	β^2	33.5 m/s

Table 2
Tunnel parameters used in the traditional 1D code (before 1:25 reduced scale).

Name	Length	Area	Perimeter	Friction coefficient	Pressure loss at entrance and exit
Tunnel	574.5 m	45 m^2	24 m	0.01	0.5

When the distance of train head inside tunnel l is long enough such that β_2' is able to fit the relationship among characteristic variables, then Eq. (14) is substituted by Eq. (15) to solve the unknown Riemann variables. β_{2S}' is calculated by interpolating β_2' at the previous moment. The last four terms in the equation represent the influence on β_2' caused by entropy, friction, heat transfer, and area change.

The deduction of boundary conditions at the train tail is similar to that at the train head. The entry of the train head into the tunnel can be simplified as airflow entering from a duct of larger cross-sectional area to a smaller one, while the train tail is the opposite. The boundary conditions at tunnel portals connect the flow between the tunnel/annulus and the atmosphere. The atmospheric pressure is set to 1 atm and the temperature is 20 °C, which is the same as the initial pressure and temperature inside tunnel. Therefore, only the three characteristic variables in the tunnel/annulus need to be solved. Specifically, for the inflow condition where air flows from the atmosphere to the tunnel/annulus, the unknown variables are solved by combining the momentum equation, thermodynamic relationship equation, and characteristic equation. For the outflow condition where air flows from the tunnel/annulus to the atmosphere, the characteristic variables A_A and λ can be directly solved from the characteristic equations. Since the pressure at the tunnel portal for the outflow condition is equal to atmospheric pressure, the characteristic variable β is obtained.

As can be seen from the equations given in the introduction to the 1D numerical model, some input parameters of describing the train and tunnel need to be pre-determined, including area/perimeters/length/frictional coefficients of the train and tunnel, as well as the pressure loss coefficient at head/tail of the train and tunnel portals. According to (Vardy and Reinke, 1999), the empirical parameter of head loss coefficient ζ_N for passenger trains is 0.005 ± 0.025, and that for freight trains is 0.01. According to the Borda–Carnot relationship, the tail loss coefficient ζ_T is $(\beta_E)^2$, in which β_E is the blockage ratio. The pressure loss coefficient at a tunnel portal is often estimated at around 0.5, which is similar to the dynamic head of a pipe inlet in a plane wall based on previous research (Woods and Pope, 1981). Details for the other parameters used in the 1D simulation of a Class 66 freight locomotive entering a tunnel are given in Tables 1 and 2.

2.3. 3D simulations

2.3.1. Numerical method

In this work, both LES and SST k-ω RANS models are adopted to simulate and analyse the flow field and to predict the development of the separation bubble. To obtain the clear shape of the separation bubble as the train enters into the tunnel, URANS (Unsteady Reynolds-averaged Naiver–Stokes) is adopted over LES. It is understood that URANS is more dissipative than LES and as such this technique is adopted to avoid the generation of a high number of turbulent flow and transient coherent structures, which mask the overall shape/size of the core separation bubble, which is the main feature creating the effective shape of the freight locomotive nose entering into a tunnel. Compared to other RANS models, k-ω SST model is expected to predict a better result for the separation bubble since it can eliminate the adverse free flow issues of the Wilcox model, and avoid overpredicting the shear stress at the train surface (Hellsten et al., 1997). To reduce the error caused by discretisation, a second-order upwind scheme is used for the discretisation of the convection and diffusion terms.

Thus the RANS approach was used for the simulation with the tunnel, including the reference simulation and the simulations to investigate the influence of blockage ratio, as the fluctuating quantities are averaged using the RANS model, which enables clear identification of the separation bubble shape at different moments when the train enters a tunnel. LES is used in the case of trains operating in an open field, including the parameterisation study due to its ability on providing more accurate predictions of vortex separation (Keogh et al., 2016; Krajnovic and Davidson, 2002; Hemida and Baker, 2010). Therefore the LES method is adopted to conduct the parameterisation study of the separation bubble size by simulating freight trains with various head shapes operating on an open field. A Wall-Adapting Local Eddy-Viscosity (WALE) model is adopted for the subgrid-scale (SGS) model in this study. Previous research shows that the WALE model performs well in resolving complex flows, including those with separation regions (Benchikh Le Hocine et al., 2019). The bounded central differencing scheme is used for the discretisation of the convection terms to ensure accuracy and stability of the simulation. For both simulations, the relevant control equations are solved using the CFD software Fluent based on the finite volume method, and a PISO pressure–velocity coupling method is also adopted. The time step Δt is set as 4×10^{-5} s, estimated by $CFL \leqslant 1$ ($CFL = \Delta t \cdot v / \Delta x_{\min}$, where v is the train operating speed and $\Delta x_{\min}$ is 0.0015 m in this paper).

2.3.2. Computational domain and boundary conditions

The commercial software Fluent is used to solve the 3D flow field and pressure wave pattern induced by a freight train entering a tunnel. A sliding mesh method is used to simulate the relative motion between the train and the tunnel. Using this method, the whole computational domain is composed of a stationary region that contains the tunnel and a sliding mesh region (the yellow region in Fig. 5) that contains the freight train and moves in the longitudinal direction with train speed 33.5 m/s. According to the expression of Reynolds number: $Re = \frac{ul}{v}$, and taking the train height H as the feature length, H = 0.16 m, the Reynolds number of the flow field around the freight train in this study is approximately 3.82×10^6. The whole computational domain is symmetrical with respect to xz plane and the freight train is located at the symmetry plane. The cell number in the stationary region and sliding region are 3.16 million and 31 million respectively. The dimensions of the computational domain and boundary conditions are illustrated in Fig. 5. In order to validate these simulations against previous experimental results, the tunnel configuration is selected to be the same as that used in the moving model experiment carried out by Iliadis et al. (2019). The cross-sectional area of the tunnel is 45 m^2 and the length of which is 574.5 m at full-scale. Interfaces of the stationary and sliding regions enable the information exchange between the stationary and moving regions. Ground, tunnel and train surfaces are set as non-slip walls.

In order to get the time-averaged flow information from the LES method that used in parameterisation study, simulations for this aspect are carried out in the open field. It is appreciated that the separation bubble will change when the train enters into a tunnel; however, our results indicate that the bubble size can be scaled to the size when train head just enters the tunnel using a scale factor obtained from the reference simulation case. Therefore, this approach to conduct a single simulation in the open field, removes the technical difficulties and requirement for many additional simulations within tunnels when considering a wide array of train designs. The dimensions of the computational domain, boundary conditions and the generic freight locomotive used in parameterisation study are illustrated in Fig. 6. The ground is set as a moving wall with the velocity set to be the same

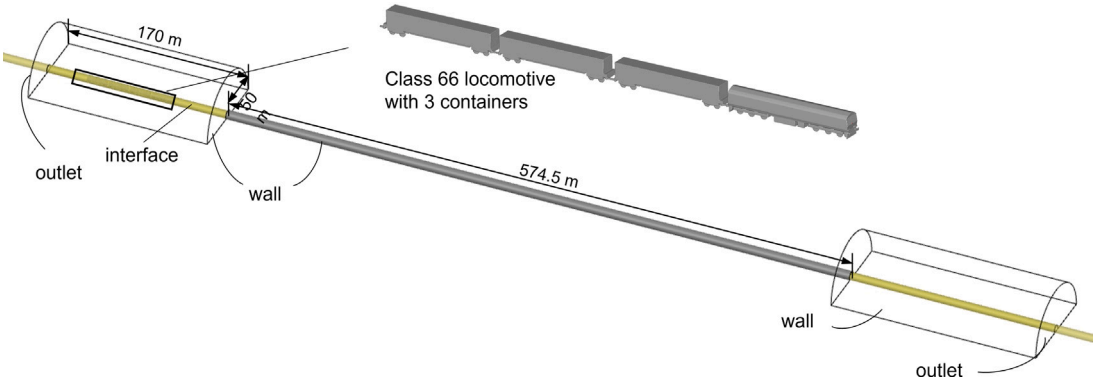

Fig. 5. Computational domain of freight train passing through a tunnel and boundary conditions (dimensions in the figure are given as full-scale).

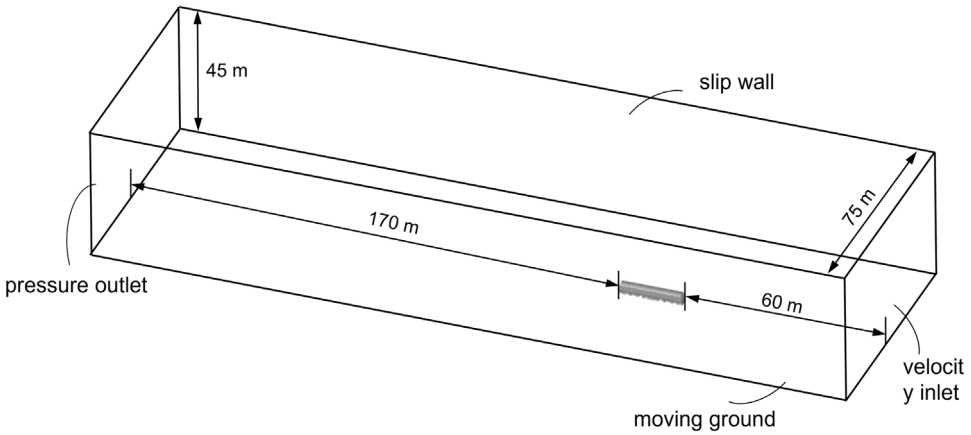

Fig. 6. Computational domain of the freight train operating in the open field and generic freight locomotive (dimensions in the figure are given as full-scale).

as train velocity, to simulate the relative movement between the train and ground. The boundaries at both sides and top planes of the open field around the train are set as slip wall to avoid the formation of boundary layers which may influence the overall flow development at these boundaries. The distance from velocity inlet/pressure outlet to the nose/tail of the freight train are set as 15/40 H respectively, to ensure the full development of the flow field.

2.3.3. Mesh

Since prediction of the separation bubble is very sensitive to the mesh quality, and subsequently the numerical model chosen, the whole computational domain is divided by a structured mesh to increase the overall mesh quality. Mesh at the region that forms after the flow separates over the leading edges of the train head is refined to resolve all motion down to the inertial subrange. The blocking structure around the train head and the mesh on train surface is shown in Fig. 7. In order to better simulate the velocity distribution in the viscous flow region of the train, the first layer of the wall of the train surface (except the bogies) is estimated with $y^+ \approx 8$ ($y^+ = \Delta y/\lambda^+$), with 17 prism layers and a total thickness of around 4 mm. According to previous research, the cell size adjacent to the wall in the spanwise and streamwise direction are $\Delta s \approx 50\lambda^+$ and $\Delta x \approx 100\lambda^+$ (Östh and Krajnović, 2014; Krajnović and Davidson, 2005b). The instantaneous wall y^+ on surface of the locomotive is plotted in Fig. 7(b) showing that it meets the requirements. A coarser prism mesh is added on tunnel and track surface. To ensure this grid size is capable of providing a sufficiently fine spatial resolution, especially in areas where the separation bubble forms, a mesh independence validation is conducted by comparing the velocity profile above the train roof with a finer mesh. For the finer mesh, the first layer of the wall is refined to $y^+ \approx 5$ with 25 prism layers. Similarly, the mesh on the train surface is refined to $\Delta s \approx 50\lambda^+$ and $\Delta x \approx 80\lambda^+$. The total cell count of the medium and fine meshes are 29 million and 36 million respectively. Fig. 8 shows a comparison of the performance of fine and medium mesh sizes in predicting the flow field using turbulence kinetic energy (TKE) and mean velocity profile. Specifically, TKE is calculated using $0.5\times(u'^2+v'^2+w'^2)$, which is used to evaluate the accuracy in predicting turbulence properties between the two mesh sizes. To provide a comprehensive analysis, data were extracted from six vertical lines located above the train roof. The x-axis values in Fig. 8(a) and (b) are obtained using the following functions: $x = x_r + 0.005 \times TKE$ and $x = x_r + 0.001 \times \bar{u}$, where x_r represents the distance from the vertical line to the leading edge, and the Z axis represents the distance to the train roof. The six vertical lines are positioned at x_r values of 0/0.04/0.08/0.12/0.16/0.2 m, respectively. Fig. 8(a) reveals that the medium mesh size slightly under predicts turbulence generation at $x_r = 0.04$ m, but the TKE data from the medium mesh size generally agree with those obtained from the fine mesh at these locations above the roof. The mean velocity profile presented in Fig. 8(a) displays minor discrepancies in the recirculation velocity within the separation bubble between the fine and medium mesh models. Both models yield identical predictions regarding the position of the boundary layer (where $\bar{u} = 0.99 \times u_{train}$) and the size (height and length) of the recirculation region, which are the parameters of interest in this paper. Therefore, the medium mesh size is adopted in this paper to complete the parameterisation study. To further confirm the adequacy of the mesh resolution and the turbulence model utilised in this study, the pressure coefficients obtained from the medium mesh are compared with the experimental results for measuring points on the train surface in Section 2.4.2.

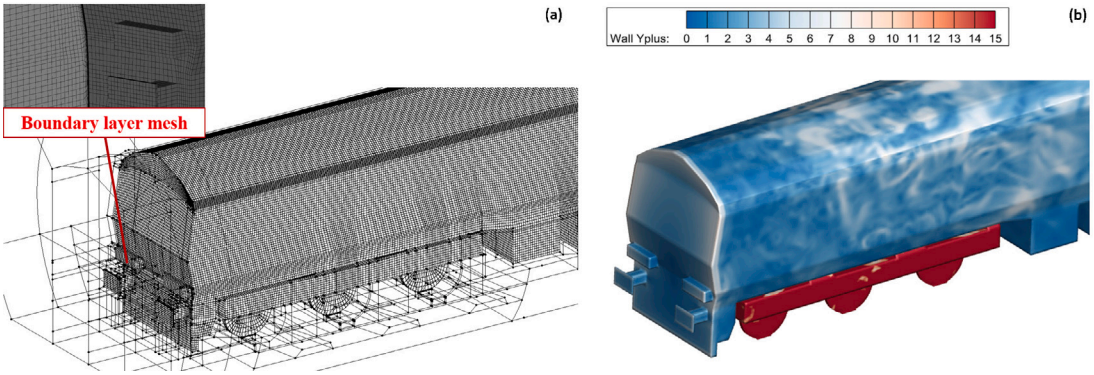

Fig. 7. Mesh size and distribution. (a) The blocking structure around the train head and mesh on train surface (b) instantaneous wall Y^+.

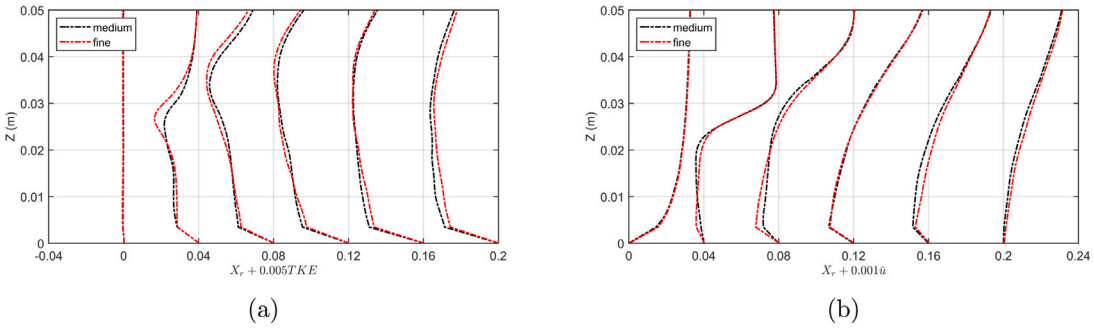

Fig. 8. Comparison between the medium and fine mesh on train roof (a) TKE (b) time-averaged velocity profile.

Table 3
Train parameters to be used for validation of the 1D code (Vardy and Reinke, 1999).

Name	Length	Area	Perimeter	Friction coefficient	Head loss	Train loss
Talgo1	146 m	10 m^2	12 m	0.003	0.075	β^2

Table 4
Tunnel parameters to be used for validation of the 1D code (Vardy and Reinke, 1999).

Name	Length	Area	Perimeter	Friction coefficient	Pressure loss at entrance and exit
Grauhoz	6298 m	62 m^2	32 m	0.006	0.5

2.4. Model verification

2.4.1. 1D code

To validate the accuracy of the 1D numerical model developed in this work, the pressure wave of a Talgo1 train passing through a tunnel predicted by this model is compared with results presented in a previous paper. The parameters adopted in the model are defined in detail by Vardy and Reinke (1999). For ease, the speed of the train is 129.5 km/h and the other main parameters of importance are listed in Tables 3 and 4. Compared to measured experimental data and previous 1D numerical results, it can be seen in Fig. 9 that the numerical model developed in this work is able to predict the magnitude and pressure wave pattern as presented by Vardy and Reinke (1999). All significant pressure signals are well predicted using this 1D model, including the compression and expansion waves caused by the entry of train head and tail, the frictional effect of train and tunnel surface, reflection of pressure waves at tunnel portal and the propagation of pressure waves inside the tunnel. It is concluded that the boundary conditions, the mesh system, the transient scheme and MOC method are successfully applied to this 1D programme.

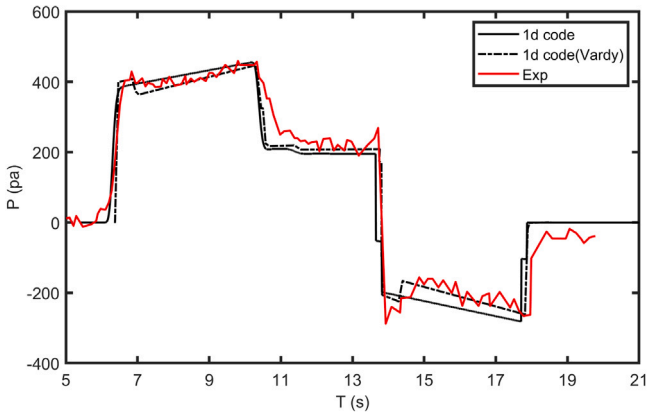

Fig. 9. Comparison of experimental results and 1d predicted pressure time history curves.

2.4.2. 3D simulation

The simulation of the freight train entering a tunnel using $k-\omega$ SST RANS model is validated against experimental data measuring using a moving model facility. The experimental setup utilises a 1/25th scale Class 66 locomotive connected to four FEA-B flatbed container wagons in a fully loaded container configuration (there are no unused container loading spaces on the wagons) passing through a 45 m^2 tunnel. Further details of the experimental settings can be found in Iliadis et al. (2019). The position of surface pressure measuring points across model train surface are illustrated in Fig. 10(a). To validate the computational simulations, pressure time–history curves at the measuring positions on train surface (P1 and P3) and on the tunnel wall 2 m inside the tunnel entrance are compared with the experimental results, as shown in Fig. 10(b). P1 and P3 are measuring points at train nose and train side located inside the separation bubble region. The pressure coefficient is

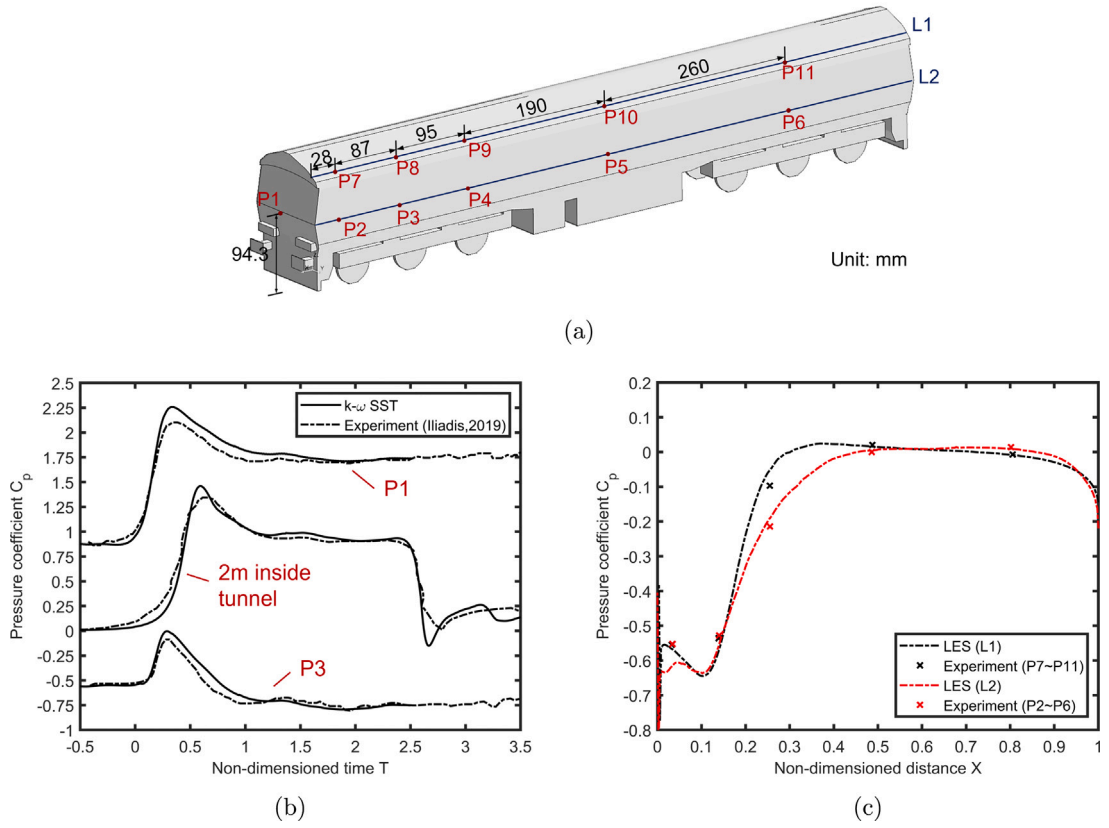

Fig. 10. Pressure history curve at measuring points (a) position of measuring points (b) comparison of pressure variation on train and tunnel surface between $k-\omega$ SST RANS and Experimental results (c) comparison of pressure distribution on train surface between LES and Experimental results.

calculated by $C_p = \frac{p-p_\infty}{0.5\rho v_{tr}^2}$ and time is non-dimensioned by $\frac{L}{v_{tr}}$, where L is the length of the locomotive. The results illustrate that the pressure at measuring points P1 and P3 before and after the train enters the tunnel are very well predicted, indicating an accurate prediction of the flow separation in this region. The maximum pressure caused by the initial pressure rise as the train enters into the tunnel is a little overpredicted by the $k-\omega$ SST model, by an error around 6%, which is typical in comparison to other studies (Ji et al., 2019; Xia et al., 2020; Premoli et al., 2016). This may be attributed to the dissipative nature of the RANS model, which tends to overestimate the size of separation bubbles. Although the $k-\omega$ SST RANS model performs better in predicting separation and reattachment of the boundary layer than other RANS models, previous research has shown that it still tends to overpredict the separation length and exhibit a lagging recovery after attachment (Kalitzin et al., 2016). In general, the computational approach performs well in predicting the effect of the separation bubble on the change of pressure wave. The results indicate that the $k-\omega$ SST model is capable of simulating the flow field pattern, providing correct flow field information (e.g. the size of separation bubble) to be fed in the parameterisation study and support the development of the 1D code for freight trains.

Finally, to validate the numerical settings and mesh resolution adopted for LES simulations, experimental results of surface pressure located at a set of measurement points along the roof and side of the locomotive are used to compare with the numerical results. Experimental data are obtained by averaging the pressure at these measurement points before the train enters the tunnel. The position of the measuring points (P2~P11 and L1~L2) used for validation is illustrated in Fig. 10(a) and the comparison of results is shown in Fig. 10(c). The X-axis is non-dimensioned by L, as per the previous definition. The pressure from the leading edge of the train head to around $0.3\sim0.4L$ is negative, indicating the separated flow region around the train nose. Measuring points P2 and P7 are located just after the leading edge separation, P3 and P8 are inside the separation region, and P4 and P9 are close to where the flow reattaches to the train body. Results show that the pressure distribution along L1 and L2 (lines located at the roof and side of the train) extracted from the LES simulation fit well with the experimental data at these points, with a percentage error below 5%. A similar conclusion can be observed at P5~P6, P10~P11 located out of the separation bubble region. Therefore, it is concluded that the simulation settings and mesh resolution adopted in the LES numerical simulations can accurately calculate the flow field information and separation region of the area of interest around the train.

2.5. Numerical cases

In order to facilitate and ease comparison between cases considered, with different train geometries, numerical models, and working conditions, Table 5 has been constructed. Operating conditions in Table 5, including tunnel/open-field and the corresponding boundary conditions, are consistent with those depicted in Figs. 5 and 6, respectively. All cases have been conducted at a Mach number of approximately 0.1, with all geometries scaled to 1/25th reduced-scale and Reynolds number calculated using the feature length H, as defined earlier, resulting in an approximate value of 3.82×10^6 across all cases. Additionally, to minimise variations attributable to meshing, a consistent blocking strategy and mesh size have been utilised for each train type to the greatest extent possible.

3. Numerical results

3.1. Reference case

Firstly, the pressure change induced by a Class 66 locomotive hauling eight intermodal container wagons entering a tunnel is modelled using the traditional 1D method, without consideration of the

Table 5
Summary of numerical cases.

Case	Geometry		Operating condition	Numerical model	Description
	Train	Tunnel			
1	Class 66 with 4 containers	45 m^2	Tunnel	1d model	Reference
2	Class 66 with 3 containers	45 m^2	Tunnel	RANS	Reference
3~8	Generic locomotive 0 + 0/15 + 0/15 + 15/30 + 0/30 + 15/30 + 30	/	Open field	LES	Parameterisation on nose bluntness
9~12	Generic locomotive 20 + 20	30/45/ 60/75 m^2	Tunnel	RANS	Parameterisation on blockage ratio
13	Class 70 locomotive	65 m^2	Tunnel	1d model	Validation
14	Class 70 locomotive	65 m^2	Tunnel	RANS	Validation

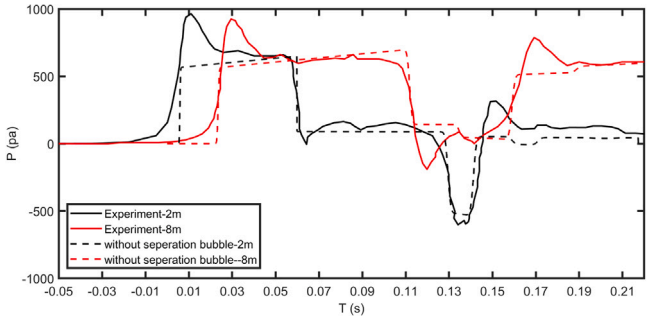

Fig. 11. Comparison of the pressure time history curves obtained from the traditional 1D modelling result and experiment data.

separation bubble model. The results for positions 2 m and 8 m inside tunnel are considered. Parameters for the Class 66 locomotive and tunnel configuration modelled in the 1D code are summarised in Tables 1 and 2. The results are then compared with the experimental data measured by Iliadis et al. (2019) as shown in Fig. 11. It can be seen that the traditional 1D methodology is able to roughly predict the trend of pressure change induced by the pressure wave formation and friction effect. However, as expected, large discrepancies occur in relation to the magnitude of the initial pressure rise, and therefore also the subsequent pressure changes as reflected pressure waves pass by the measuring points. The maximum pressure rise calculated by the traditional 1D method is 563 Pa, resulting in an error of 43% compared to that obtained from the experiment. Clearly without appropriate consideration of the separation bubble, the traditional 1D methodology has failed to predict the maximum pressure rise.

To understand the development of the separation zone at the nose of the Class 66 locomotive, and the influence this has on the pressure wave formation in the tunnel, a 3D simulation was undertaken to visualise the flow field at the blunted train nose. Streamlines around the nose of the locomotive are plotted to visualise the development and evolution of the separation region, as shown in Figs. 12 and 13. The velocities used to plot the streamline visualisation are stationary relative to the train. Velocity contours at the top ($y = 0$ m), side ($z = 0.1$ m) and bottom ($z = 0.05$ m) of the train are analysed to obtain the bubble size in each region. It can be seen that part of the flow in the separation bubble is blocked by the tunnel entrance as the train head enters into the tunnel. It not only significantly decreases the bubble size, but also increases the effective length influenced by separation bubble. The bubble size before and after the train nose enters into the tunnel are measured as shown in Fig. 13. These values are the basis for development of a separation bubble model. The results show a substantial reduction in the size of separation vortices at all locations considered. Specifically, the roof and windshield regions experienced a reduction of 33.3% and 40.5% respectively, while the bogie region had a larger reduction percentage of 52%. As the position approaches the ground, a larger portion of the airflow's motion inside the separation bubble is blocked at the tunnel entrance due to the floor as well as the tunnel wall which is closer to the train due to the tunnel shape considered, resulting in a more prominent reduction in the bubble size after it enters the tunnel.

The results obtained from these simulations are used to develop a mathematical equation for the shape of the separation bubble, which can be implemented into a redeveloped 1D model. A simplified model is built, as shown in Fig. 14, to calculate and parameterise the maximum effective blockage area. The separation region at the roof/windshield/coupling are simplified as a half circle/rectangular/rectangular shape respectively, as shaded by the blue, green and grey regions in Fig. 14. To extract the input parameters used to calculate the area of each region, $\overline{H_R}$, $\overline{W_S}$, and $\overline{W_B}$ (as shown in Fig. 14) are estimated by averaging the bubble width inside the tunnel obtained from the simulation. Thus, the maximum effective blockage area E_{max} can be calculated by summation of all components. Subsequently, the radius of the separation bubble r_b can be obtained from $E_{max} = \pi(r_t + r_b)^2$. The shape of the bubble in the streamwise direction is described as a sin function or a combination of two sin functions, as illustrated in Fig. 14(b). L_b is the bubble length around the nose and is averaged from the simulation, and the maximum effective cross-sectional area is set as $x = L_b/2$. The length of the separation bubble in the open air recovered from E_{max} to E_{train} is around $L_b/2$, labelled as separation bubble1. However, considering the suppression of the separation bubble caused by the tunnel entrance, the recovering length when the freight train enters the tunnel is longer than the open air length of the separation bubble. Therefore, the shape of separation bubble2 uses a recovering length of $3L_b/2$, which makes the total effective bubble length of $2L_b$. The parameters for the size of the separation bubble are given in the table in Fig. 14. Other parameters for the locomotive and tunnel are the same as those presented in Tables 1 and 2. Besides, from the dimensions of the side view of the freight train given in Fig. 1, the cross sectional area of a fully loaded container is smaller than the locomotive. Therefore a smaller effective area, $E_{con} = 9.5$ m^2, is adopted for the containers.

The pressure variation inside the tunnel at measuring positions 2 m, 4 m, 8 m and 16 m from the tunnel entrance portal are predicted by the redeveloped 1D model with consideration of the separation bubble. The results are compared with the same experimental results as before (Iliadis et al., 2019), as shown in Fig. 15. The red/blue dashed vertical line represent the pressure change caused by the compression/expansion waves generated by the freight train nose entering the tunnel and the reflections when the pressure waves reach the tunnel portals. Black vertical lines represent the head of the locomotive passing the measuring point of consideration. It can be seen that by adding the influence of the separation bubble, the error of the maximum initial pressure rise is reduced to 4% in comparison to the experimental results, rather than the error of 43% observed through the traditional 1D model. Furthermore, the subsequent pressure changes caused by the reflected pressure wave from tunnel exit are also well predicted. The pressure drop when the train head passes the measuring point at 2 m is however over predicted by the 1D model. This is due to the large difference in pressure variation over the separation bubble caused by a strong 3D effect for the region very close to the tunnel entrance, which is not able to be fully captured in a 1D model. For the measuring position of 4 m from the tunnel entrance, the difference between the experimental data and the result from the 1D model prediction of the pressure drop caused by train head is greatly reduced.

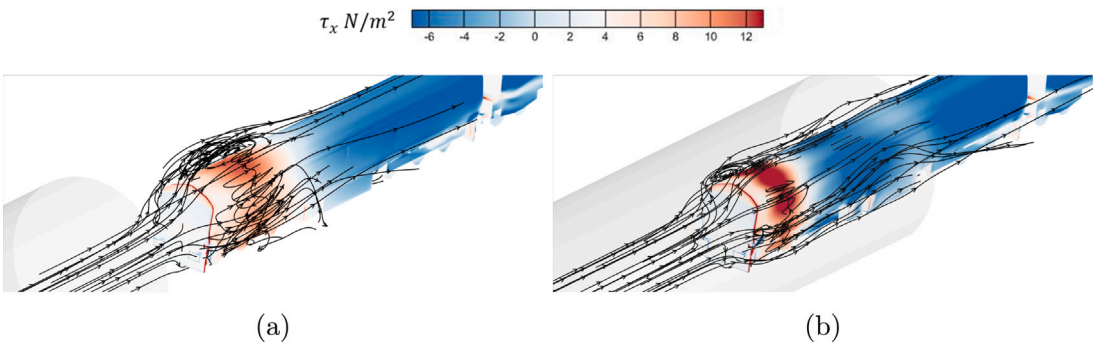

Fig. 12. Flow field around Class 66 locomotive (a) before entering the tunnel (b) after entering the tunnel.

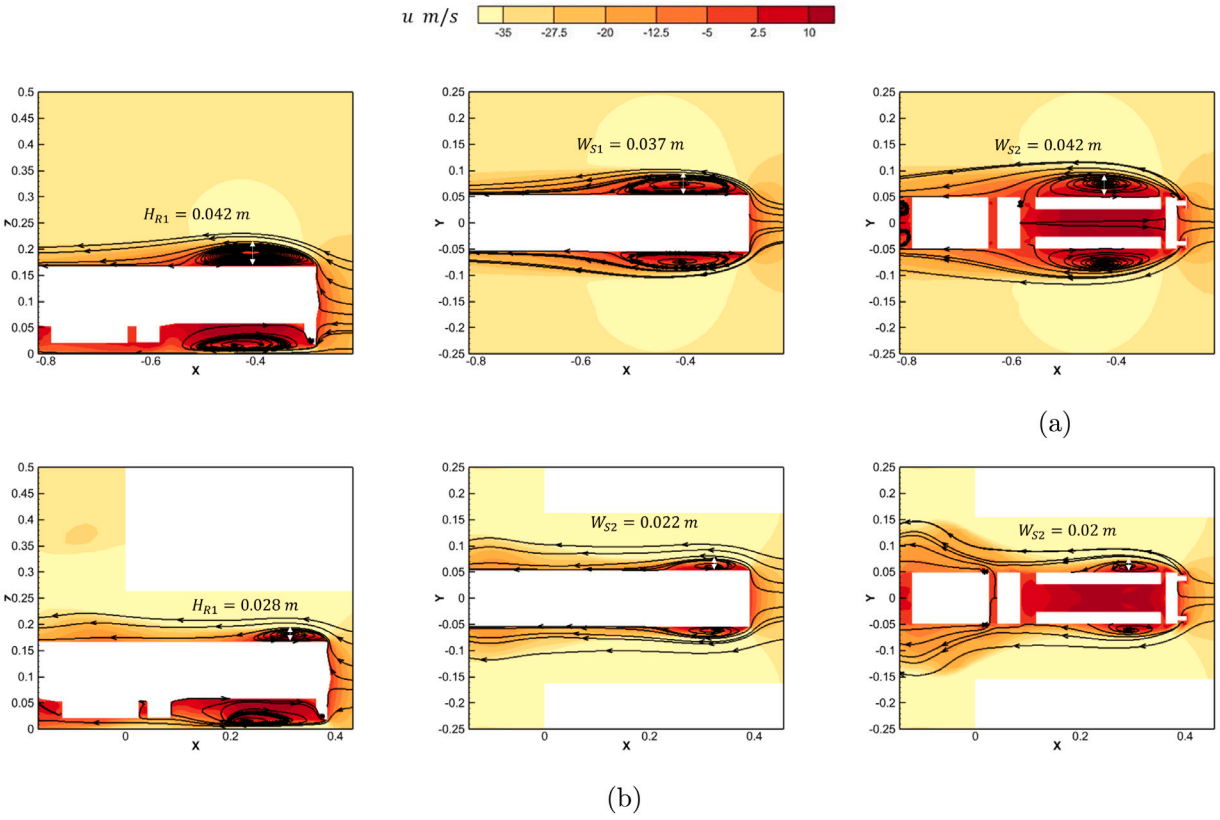

Fig. 13. Separation bubble size at top, side bottom of the train nose (a) before entering the tunnel (b) after entering the tunnel.

3.2. The effect of bluffness

From the discussion above, it can be seen that the prediction of tunnel pressure wave formation, including the maximum pressure, can be greatly improved for bluff freight vehicles by appropriately implementing the size of the separation bubble into the 1D model. To improve the functionality of this redeveloped 1D model to apply to various types of freight train design, a parameterisation study of the separation bubble is undertaken by investigating the effect of the bluffness of the locomotive. Whilst it is acknowledged that this approach is initially computationally expensive, the ability to accurately numerically model pressure waves through a 1D methodology will enable a wider range of train types and tunnel configurations to be examined. As discussed in Section 2.1, it is observed that for the range of typical European freight locomotives examined, the different shapes of freight locomotive head can be divided into three parts: roof, windshield, and coupling region, in line with standards on train design and gauging. Here analysis is conducted to investigate the influence of characteristic angles connecting each part on the height and width of the separation bubble formation. The geometries used for the parameterisation study are given in Section 2.1.

3.2.1. Wall shear stress

Time-averaged trace lines and wall shear stress on the surface of the different locomotives, at the roof and train side, are presented in Fig. 16 and Fig. 17 respectively. The computation of trace lines on a wall surface is accomplished by employing the wall shear stress in three dimensions, which is closely tied to the velocity gradient at the first grid layer near the wall due to its definition. The velocity gradient at the wall surface governs both the direction and magnitude of the velocity vector, which in turn dictates the flow characteristics and thus are utilised to generate the trace lines. Wall trace lines are commonly adopted in previous research to identify regions of separation, reattachment, and other flow features (Krajnović and Davidson, 2005a,b; Chen et al., 2019). The results clearly show the difference in the direction of the flow and the position of the separation bubble caused

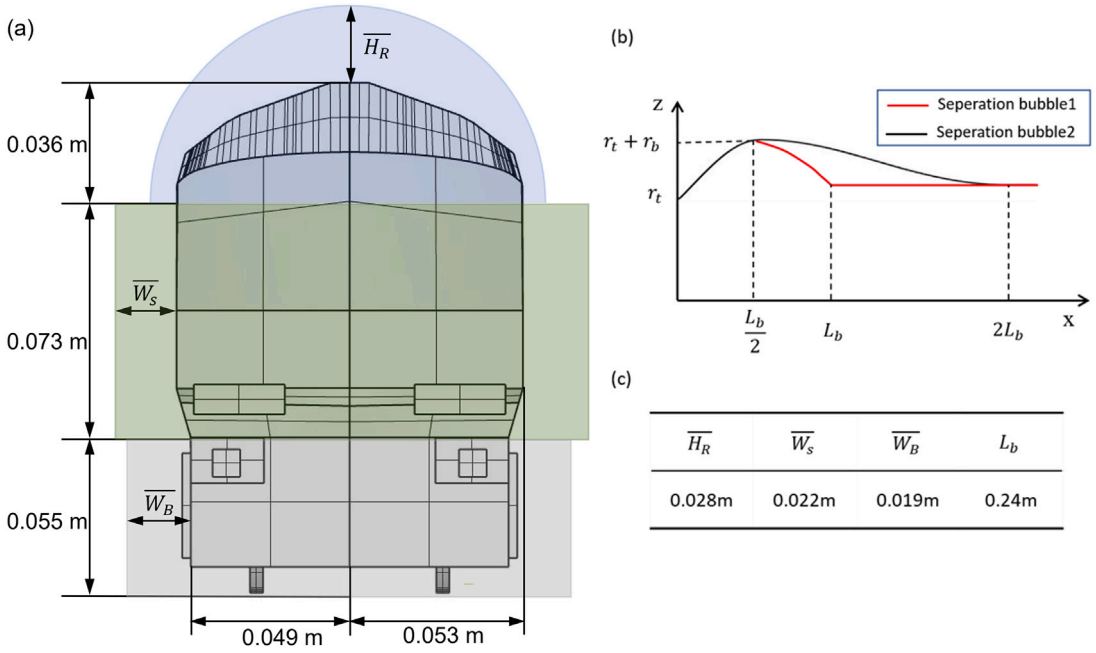

Fig. 14. Separation bubble model at the head of the Class 66 locomotive (a) effective blockage area (b) effective bubble length (c) parameters of the size of the separation bubble adopted in the code.

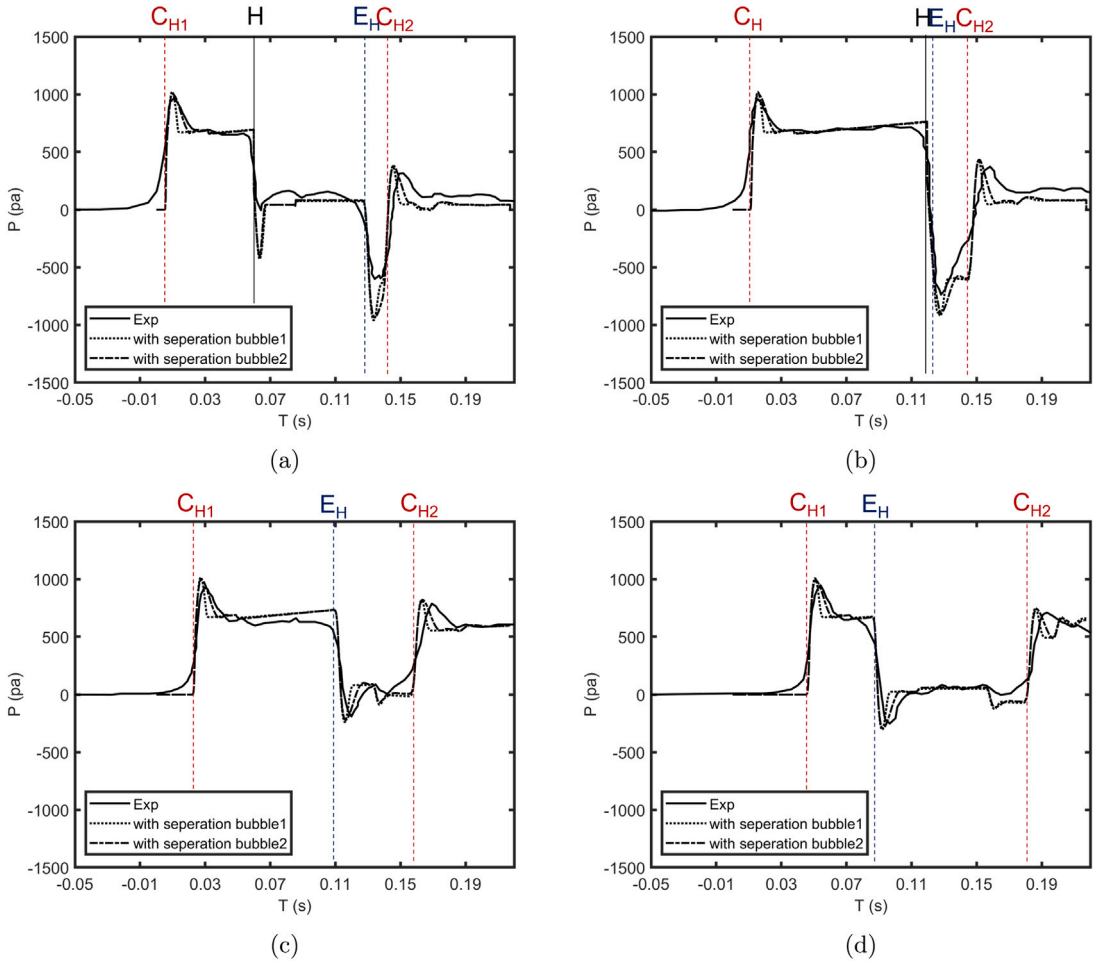

Fig. 15. Comparison of pressure time history curves obtained from 1D result and experiment data (CH1: the first compression wave induced by the train head entering the tunnel; EH1: Expansion wave when CH1 reflected back from the tunnel exit; CH2: the second compression wave when EH1 reflected from the tunnel entrance; H: the head of the train).

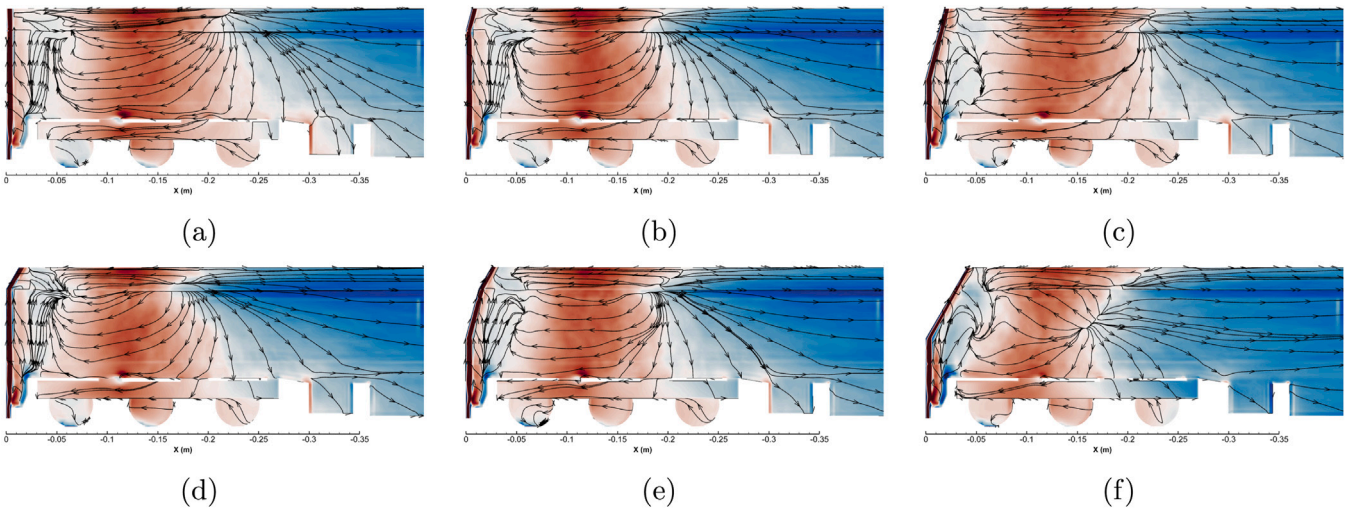

Fig. 16. Top view of time-averaged trace lines on the train body.

by the change of bluffness. From the figures, it is possible to observe the bifurcation lines, where 'the lines are drawn in the flow toward which the trajectories are asymptotic' (Perry and Chong, 1987). More specifically, positive bifurcation lines (PBL: flow separate from the line) and negative bifurcation lines (NBL: flow goes into the line) indicate where flow is separated or is attached. The length of the separation bubble is defined as the length from the train body leading edge to where the mean shear stress of x-direction equals zero. The results are measured and summarised in Table 6. The lengths of the separation bubble on the roof (L_R1) and corner (L_S1) are non-dimensioned by the width of the train (W).

It can be seen from Fig. 16 that the bluffness does not show much impact on the overall composition of the flow region at the train roof, but it does have an impact on the strength of the recirculating flow and the length of the separation bubble. In general, as the air flows over the leading edge, it creates a thin recirculation region, with a distinct separation bubble region between PBL and NBL, where the wall shear stress shows as red in the figures. As the leading separation angle (α) increases, the colour where the separation bubble exists is lighter, indicating a smaller recirculating flow velocity close to the train surface and a weaker concentrated vorticity field. Additionally, the unstable node (UN) moves sideward. From Table 6, it can be seen that, in general, the length of the separation bubble on the roof (L_R) decreases as the leading edge angle (α) increases. However, it also shows a trend of slightly increasing as the sub-angle (β) increases. This is thought to be due to the longer slope accelerating the air before it reaches the leading separation edge. Further analysis will be considered by extracting the velocity profile along the roof in Section 3.2.2.

From the side view of the time-averaged trace lines on the train body, a more obvious difference can be observed when the sub-angle (β) increases. As marked in Fig. 17(c), when β increases the position of NBL changes from the top corner to the middle height of the locomotive. Unlike other cases, a more significant difference is observed for the 30+30 case, in that the stable node transforms into a stable spiral at the front of the locomotive. Furthermore, the position of the node source, where the length of the side separation bubble is the shortest, moves from the upper corner to the middle height of the train, as shown in Fig. 17(f).

3.2.2. Streamline and velocity field

The time-averaged streamlines at the front of the locomotive with different bluffness are compared on $Y = 0W$ and $Z = 0.6H$ planes, to visualise the distribution of the separation bubble as shown in Figs. 18 and 19. To be more specific, the flow field is coloured by mean velocity

Table 6
The length of the separation bubble at train roof and side.

	0 + 0	15 + 0	15 + 15	30 + 0	30 + 15	30 + 30
L_{R1}/W	2.008	1.788	1.951	1.694	1.737	1.735
L_{S1}/W	1.782	1.521	1.632	1.483	1.381	1.035

in the longitudinal x-direction, whereby the region coloured in red is where the speed is positive, indicating a back flow or separation region.

The overall height of the separation bubble in the middle of the top of the train is larger than that on the $Y = 0.4W$ plane. Similarly, except for the 30 + 30 case, the width of the vortex on the middle height of the train is larger than that on the $Z = 0.9H$ plane (near the corner). This phenomenon is consistent with the previous results for the trace lines on the train body, in that, except for the 30 + 30 case, the shortest vortex length is at the upper corner of the train. To quantitatively compare the difference across different train bluffness and understand the relationship between the bubble size and geometrical angles, the results of the bubble size are measured from the figures and summarised in Table 7. Subscript $R1, R2, S1, S2$ represent the position at plane $Y = 0$, $Y = 0.4W$, and $Z = 0.6H$, $Z = 0.9H$ respectively. The sizes of the separation bubble are non-dimensionalised by W. Among all cases, the separation bubble generated by case 1 is the largest at all planes investigated. The height of the vortex at the top and side of the locomotive decreases when the leading separation angle α increases. Comparing the size of the separation bubble at the middle of the roof (H_{R1}) for Fig. 18(b), (c), and (d), (e), and (f), it can be seen that H_{R1} is not sensitive to sub-angle β. However, H_{S1}, which is the width of the bubble at around the mid-height plane Z=0.6H, significantly decreases with the increase of sub-angle β. This trend is the opposite for H_{S2} at plane Z=0.9H, which is the upper corner of the locomotive. This is thought to be related to the source point on the train roof moving sidewards when increasing sub-angle β (as shown in Fig. 16). In order to further analyse how the geometrical angles influence the flow and the formation of the separation bubble, the mean velocity distribution along a set of vertical lines above the roof are compared in Fig. 20. It can be seen that changing the bluffness of the train head mainly has an influence on the velocity at 0.04 m from the leading edge where the flow has just separated. Fig. 20(a) shows that increasing α can significantly decrease the height of the recirculation area, but this also has the effect of increasing the recirculation velocity. A similar conclusion can be deducted from Fig. 20(c) when β and α increases at the same time. Increasing β will increase the recirculation velocity and at the same time slightly increase the height of the separation region close to the leading edge. This is again thought to be due to the acceleration of the airflow caused by the longer slope at train head.

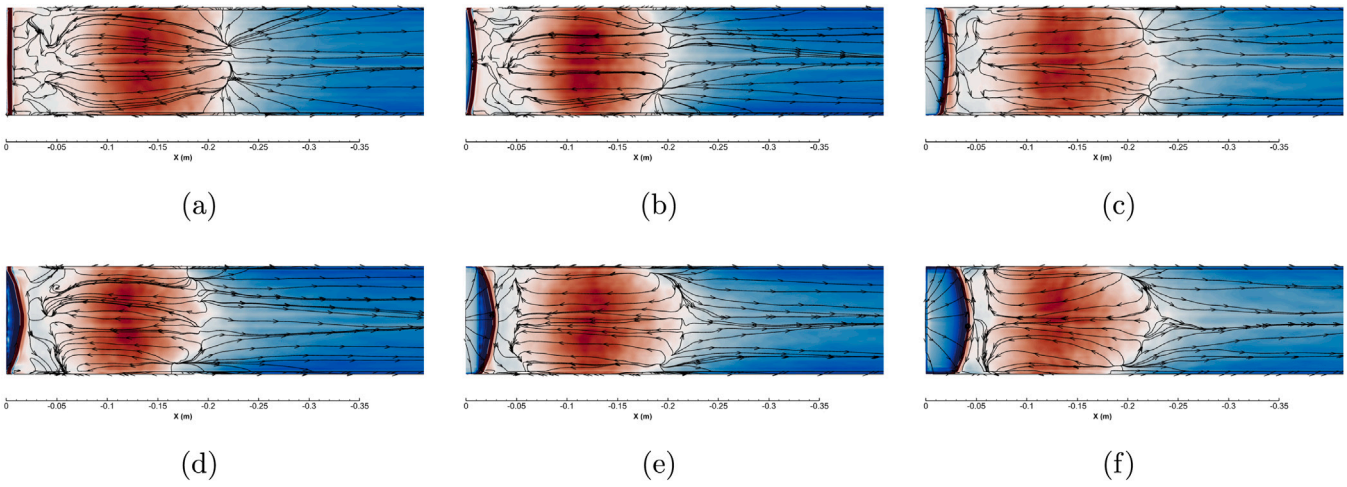

Fig. 17. Side view of time-averaged trace lines on the train body.

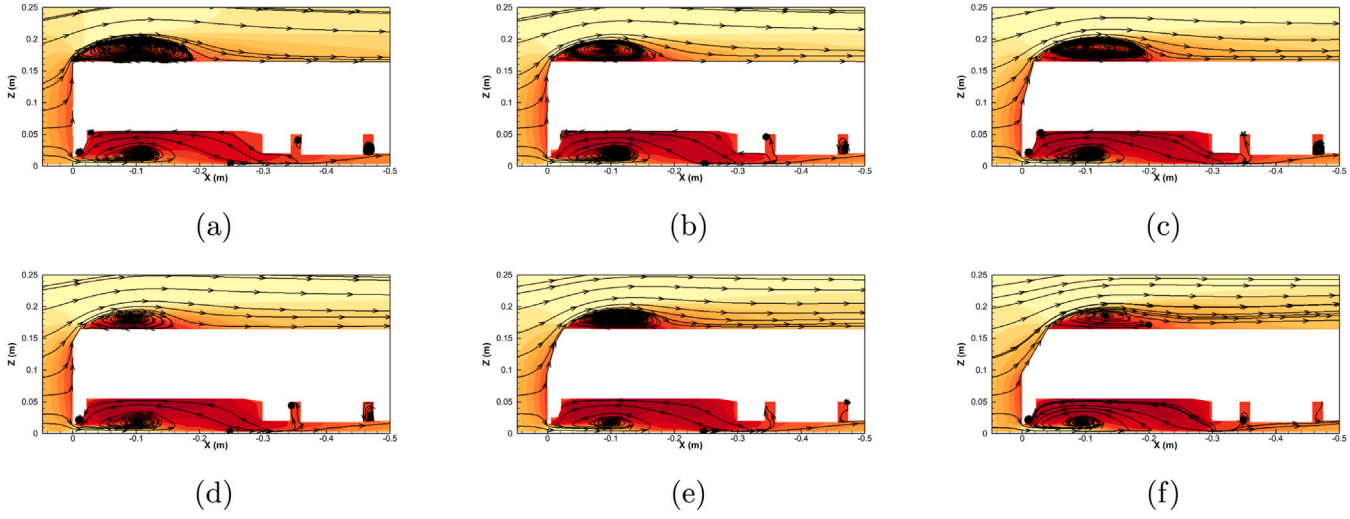

Fig. 18. Time-averaged streamline at plane $Y = 0$ m.

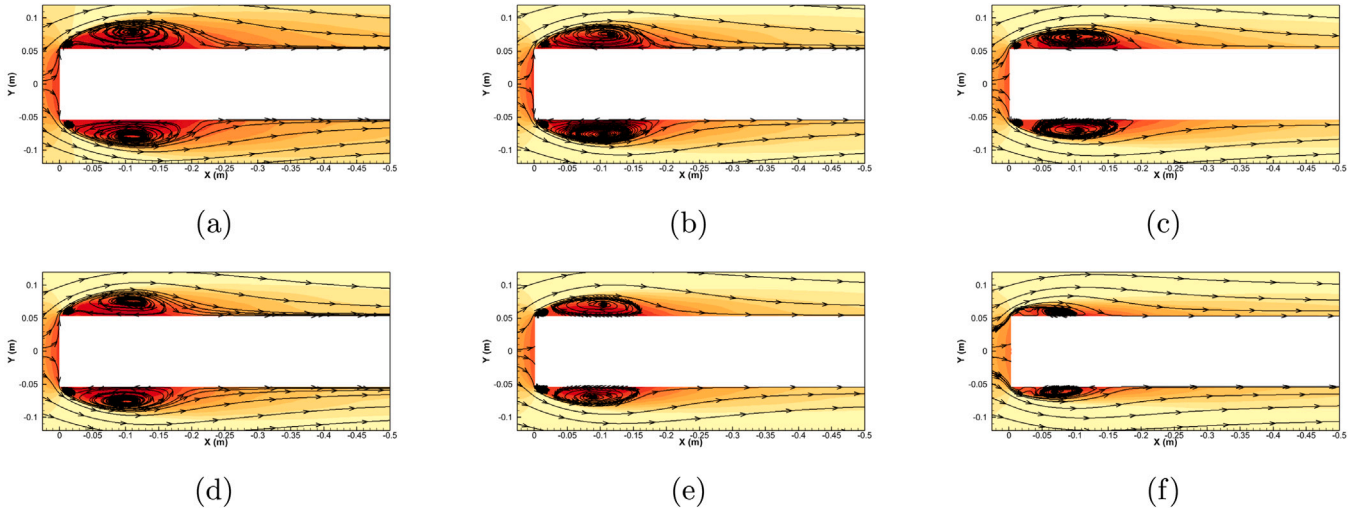

Fig. 19. Time-averaged streamline at plane $Z = 0.6H$.

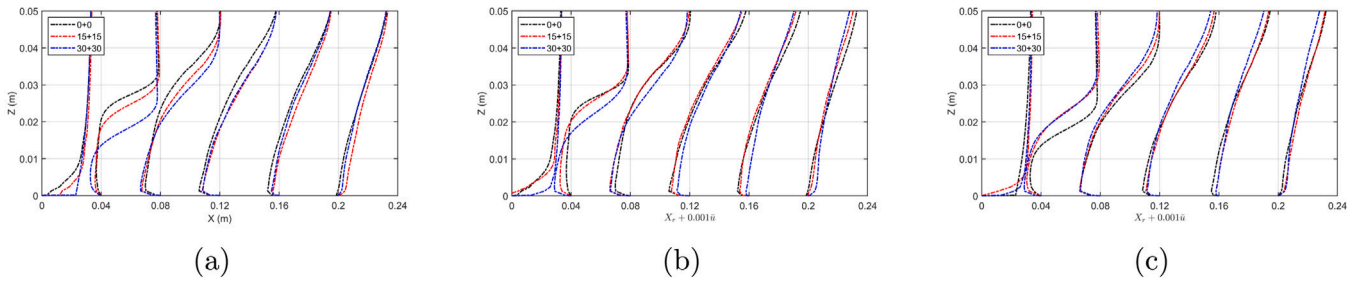

Fig. 20. Time-averaged velocity profile above the train roof (a) influence of α (b) influence of β (c) influence of $\alpha + \beta$.

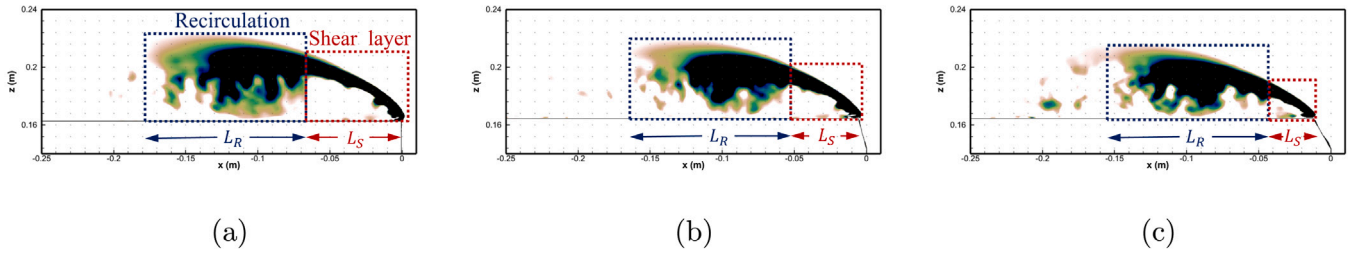

Fig. 21. Mean λ_2 at the top of the train (a) 0 + 0 (b) 15 + 0 (c) 30 + 0.

Table 7
The size of the separation bubble for six different train bluffness ratios in different measurement planes.

$\alpha+\beta$	0 + 0	15 + 0	15 + 15	30 + 0	30 + 15	30 + 30
H_{R1}/W	0.406	0.331	0.350	0.285	0.294	0.275
H_{R2}/W	0.257	0.219	0.238	0.145	0.154	0.135
W_{S1}/W	0.429	0.382	0.336	0.359	0.299	0.196
W_{S2}/W	0.280	0.196	0.280	0.149	0.215	0.243

3.2.3. Vortex structures

Previous literature has elucidated the physical phenomenon of the separation and reattachment of flow around bluff bodies (Rocchio et al., 2020). Briefly, the flow initially separates from the upstream leading edges, leading to the formation of a separated shear layer (Region I). This separated layer subsequently undergoes roll-up, generating instantaneous vortex structures of varied sizes, resulting in a recirculation region (Region II) in mean flow visualisation. These regions are demarcated by red and blue dotted squares in Figs. 21 and 22. The time-averaged λ_2 is calculated to identify the vortex structures on the top and side of the train. The Lambda-2 criterion involves analysing the second eigenvalue of the velocity gradient tensor, which reflects local rotation and stretching of fluid elements. Vortex cores are identified where the second eigenvalue is negative and the magnitude of the velocity gradient tensor is large. Given that the results above have indicated that the vortex on the roof is more susceptible to changes in α, while the vortex on the side of the train is more sensitive to variations in β, comparisons for the former are made by varying α in Fig. 21, whereas the latter is performed by varying β in Fig. 22. As anticipated, the observed results demonstrate that the increase in α has a notable impact on reducing the length of the shear layer region (l_s) and the height of the recirculation region (l_h). More specifically, the l_s is observed to decrease from 0.07 m to 0.045/0.03 m when α increases from 0 to 15/30°. On the other hand, the impact of β on the vortices observed at the side of the train is found to be more significant. Upon increasing β, the dimensions of both regions, l_s, h_s, l_r, and h_r, experience a notable reduction as shown in Fig. 22.

Previous research has suggested that the vortex structures present on a train's roof are sensitive to changes in the head bluffness, particularly variations in α. To further investigate the impact of bluffness on vortex instability, a Fourier transform velocity frequency analysis was conducted on a set of points located just beyond the mean average shear layer edge. This methodology is proposed by Rocchio et al. (2020) to analyse the Kelvin–Helmholtz instability onset. Specifically, measurements were taken at ten points along the x-axis (f1–f10 in Fig. 23), with a spacing of 0.01 m between each point, covering a range from 0 to 0.09 m from the train head. The amplitudes of the spectral density obtained from the Fourier transform were shifted linearly to allow for comparison among the set of measuring points, and to enable observation of the frequency changes associated with vortex evolution. The frequency are non-dimensionalised by W and train velocity $v_t r$, and expressed as Strouhal number $St = fW/V_{tr}$, which is the x-axis in Fig. 23.

As shown in the figure, the frequencies where peak occurs changes from f_{KH} to $f_{KH}/2$ and $f_{KH}/4$ when measuring points moving from f1 to f10,indicating the pairing of vortical structures that originate from the roll up of the shear layer as the flow moves downstream. Here, f_{KH1}, f_{KH2} and f_{KH3} represent the Kelvin–Helmholtz frequency for α = 0, 15 and 30, respectively. Peaks for $f_{KH1}/f_{KH1}/2/f_{KH1}/4$ are found at measuring points f2–f7/f6–f9/f9–f10, corresponding to a distance to the leading edge in the range of [0.01,0.06]/[0.05,0.08]/[0.08,0.09] m. Similarly, peaks for $f_{KH3}/f_{KH3}/2/f_{KH3}/4$ are found at measuring points f1–f6/f3–f8/f6–f9, corresponding to a distance to the leading edge in the range of [0.0,0.05]/[0.02,0.07]/[0.05,0.08] m. These results indicate that the shear layer roll-up and form vortices earlier (closer to the leading separation edge) when α increases, which is consistent with the phenomenon observed in Fig. 21. The magnitude of these Kelvin–Helmholtz frequencies does not exhibit a significant change with the alteration of α. Specifically, f_{KH1} and f_{KH3} slightly decreases from 3.54 and 3.34 when α increases from 0 to 30°.

3.3. The effect of blockage ratio

The separation bubble model, discussed in Section 3.1, incorporates a scaling factor for the size of the separation region when transitioning from an open field to a tunnel. In order to establish the generalisability of the model across different scenarios, an investigation was carried out to examine the correlation between the scale factor and the blockage ratio β_E. The investigation involved examining various tunnel cross-sectional areas (30/45/60/75 m^2), corresponding to β_E values ranging from 0.14 to 0.35, chosen to represent a range of tunnel sizes that necessitate accounting for the aerodynamic effect of freight trains.

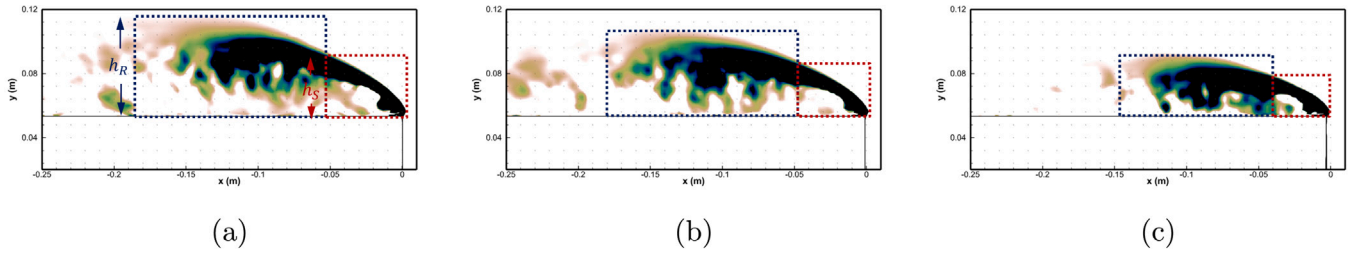

Fig. 22. Mean λ_2 at the side of the train (a) 30 + 0 (b) 30 + 15 (c) 30 + 30.

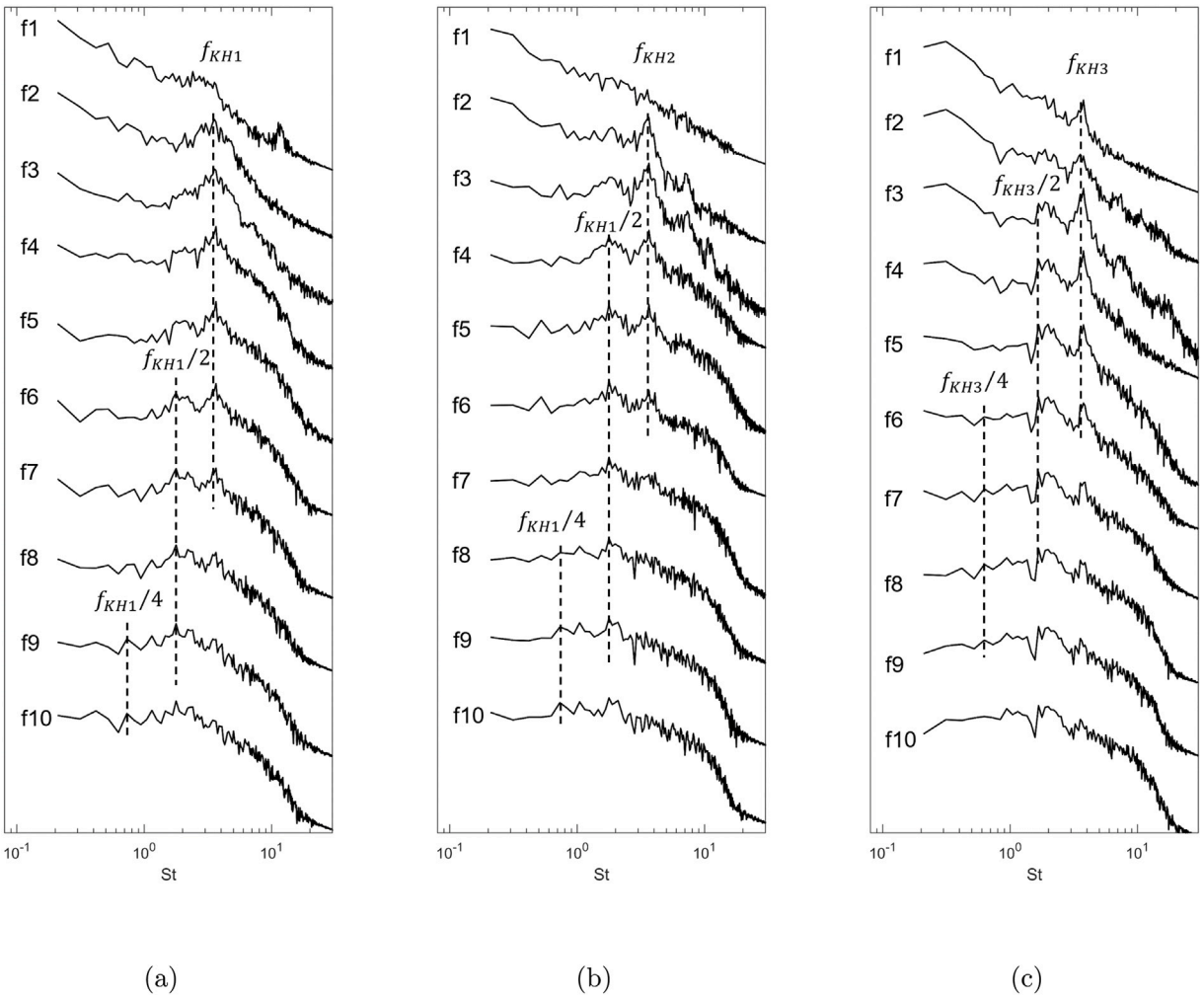

Fig. 23. PSD of velocity fluctuations at positions near average shear layer edge (a) 0 + 0 (b) 15 + 0 (c) 30 + 0.

In this investigation, the separation bubble's height on the roof, side, and bottom of a freight train inside a tunnel was measured using the methodology proposed in Section 3.1. The relationship between the scale factor of $H_R/H_{S1}/H_{S2}$ and β_E was graphically depicted in Fig. 24. The configuration of the train and tunnel indicated that as the cross-sectional area of the tunnel decreases, the space between the roof of the freight train and the tunnel ceiling decreases at a faster rate than the space between the side of the freight train and the tunnel sidewall. This limited space at the top exerts a stronger squeezing effect on the separated region above the roof, which may be the reason for the slightly faster decrease rate of H_R compared to H_{S1} and H_{S2} as β_E increases. In general, the results indicate that within the range examined, the scale factor of these three variables decreases linearly, with a similar decreasing rate, as β_E increases. As such, for ease of model application, the radius of the separation bubble r_b (as shown in Fig. 14), which accounts for the overall influence of the separation region on the effective cross-sectional area, was investigated instead. The relationship equation between the scale factor of r_b and β_E is given in Fig. 24(b).

3.4. Parameterisation equation

Now that the results for the influence of train nose bluffness and tunnel geometry have been considered it is important for the development of the 1D model to draw all this information together into a parameterisation equation. A parameterisation equation is obtained by using polynomial fitting function to get the relationship between the bubble height on roof and the side of the train with the angles (α and β) controlling the bluffness of the head. The angles are transformed to

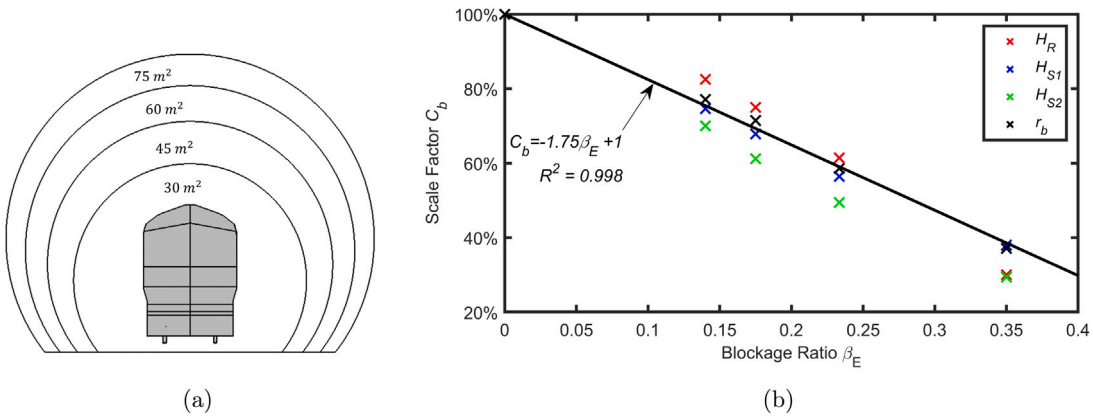

Fig. 24. Influence of the blockage ratio on the scale factor. (a) Configuration of the tunnel cross section (dimensions given as full-scale) (b) Relationship between r_b and β_E.

Table 8
Fitting parameters for the parameterisation equation.

	h0	$C_{\alpha 1}$	$C_{\beta 1}$	$C_{\alpha 2}$	$C_{\beta 2}$	R-Square
H_R/W	0.406	−0.318	0.1213	0.1568	−0.259	0.9980
H_S/W	0.429	−0.1919	−0.1003	0.0985	−0.390	0.9985

Table 9
The relative position of the vortex core with respect to the full height and length of the vortex (%).

$\alpha+\beta$	0 + 0	15 + 0	15 + 15	30 + 0	30 + 15	30 + 30
H_C/H_R	49.43%	54.93%	60%	57.38%	62.54%	67.46%
L_C/L_R	47.38%	46.44%	48.77%	42.94%	47.81%	48.06%

radians before fitting into the equation. The equation used to fit the variables is given in Eq. (18) and the fitting parameters are given in Table 8. The R-Square of both fitting functions fall in the range over 0.998, indicating a strong relationship between the fitting model for the bubble height and the variables that control the bluffness of the train head. The fitting domains that show the relationship between the height of the separation bubble (H_R and H_S) and the bluffness of the train (α and β) are shown in Fig. 25. From the parameters and the fitting domain, it can be seen that, as analysed in Section 3.2.2, the size of the separation bubble on the roof is more sensitive to α. However, the height of the separation bubble on the side of the train exhibits a more obvious trend of decrease when β increases. In order to assess the influence of α and β on the separation region, a sensitivity analysis is performed using Sobol indices. Total-order Sobol indices are calculated to determine the extent to which the total variance of H_R and H_S can be attributed to α and β, taking into account both the direct and indirect effects. The range of α and β values considered is [0,0.0524] radians. The total-order Sobol indices of α and β for H_R are found to be 0.975 and 0.05, respectively. These results indicate that around 97.5% of the total variance in H_R can be explained by variations in α, indicating that α has a more dominant impact on the separation height at the roof of the train than β. For H_S, the total-order Sobol indices of α and β are 0.172 and 0.828, respectively, indicating that approximately 82.8% of the change in H_S can be attributed to variations in β.

$$\mathrm{H}(\alpha,\beta) = \mathrm{h0} + \mathrm{C}_{\alpha 1}\alpha + \mathrm{C}_{\beta 1}\beta + \mathrm{C}_{\alpha 2}\alpha^2 + \mathrm{C}_{\beta 2}\beta^2 \quad (18)$$

Previous research has shown that the shape of locomotive head has a significant impact on the length and width of separation regions (Lunghi et al., 2022). This study further analyses the height and length of the centre of the separation bubble (H_c and L_c) at the top of the train. The relationship between H_c and L_c with α and β is presented in Fig. 26. The results indicate that both H_c and L_c increase as α decreases and β increases. This trend is consistent with the influence of bluffness on the full height and length of the separation region (H_{R1} and L_{R1}) at the top of the train. Table 9 summarises the relative position of the vortex core with respect to H_c and L_c. The findings show that the relative height of the vortex core significantly increases with an increase in α and β, while the relative length of the vortex core does not change much with a variation in bluffness. The relative length slightly increases as β increases and α decreases, with the percentage position change ranging from 40% to 50%.

3.5. Validation of the model

To assess the validity and applicability of the relationship equations detailed in Section 3.3, Section 3.4, and the proposed separation bubble model outlined in Section 3.1, an additional simulation was conducted featuring a Class 70 locomotive (Fig. 27(a)) passing through a 65 m^2 tunnel. The locomotive surface mesh and the dimensions for the roof/windshield/coupling regions required for the separation bubble model are illustrated in Fig. 27(b). Due to the unique design of the Class 70 locomotive, as depicted in Fig. 27(a), separate cross-sectional area are used for the locomotive's head (9.5 m^2) and body (8.5 m^2). It is worth noting that these dimensions are obtained directly from the locomotive's CAD model.

To calculate the height of the separation bubble at the roof and windshield regions of the Class 70 locomotive head, the parameterisation equation is utilised with values of α and β equal to 12°. The resulting separation bubble height values are then inputted directly into the separation bubble model to calculate the recirculation region in the open field, $H_R = 0.36W$ and $H_S = 0.355W$. Subsequently, the effective area within the tunnel is determined by scaling down the effective blockage area in the open field using the reduction factor C_b, specific to the 65 m^2 tunnel cross-sectional area, calculated using the equation presented in Fig. 24. With $\beta_E = 0.146$, the calculated value of C_b is found to be 0.74.

To evaluate the performance of the proposed methodology, the pressure time history curves obtained from the redeveloped 1D numerical model are compared against the CFD results for distances of 8 m and 16 m from the tunnel entry portal, as shown in Fig. 28. It can be observed that the magnitude of the maximum initial pressure rise obtained from the 1D model is in good agreement with the CFD simulation results for the validation case. Moreover, the peak values caused by compression and expansion waves, as well as the pressure changes caused by the reflected pressure waves, are also accurately predicted. Hence, it can be concluded that this additional simulation successfully validates the accuracy of the relationship equations and the separation bubble model in predicting the pressure wave formation and behaviour for a Class 70 locomotive passing through a tunnel.

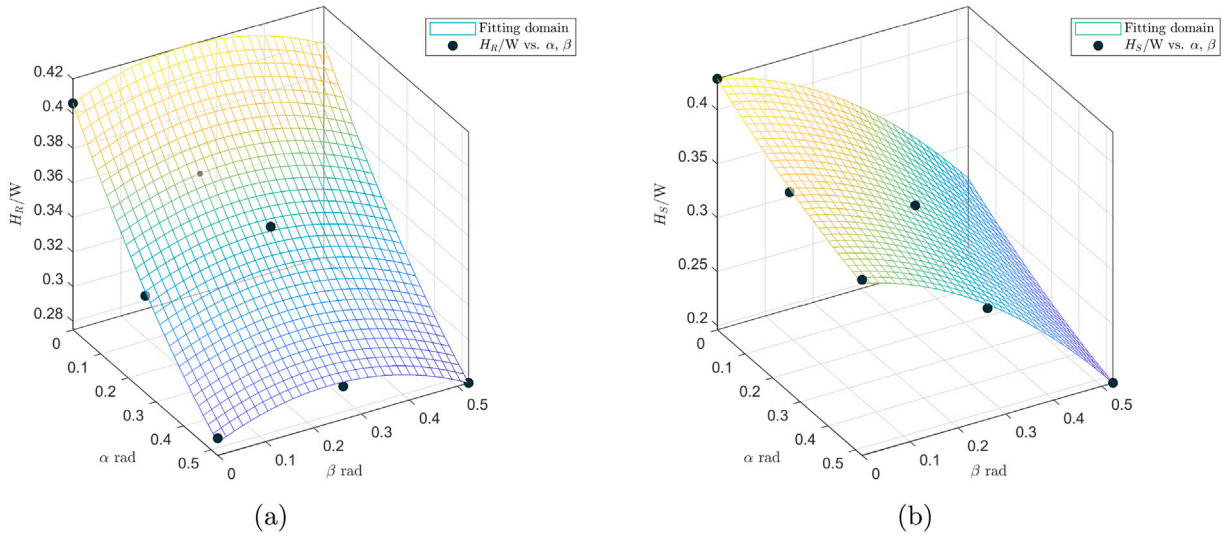

Fig. 25. Fitting domain for the height of separation bubble and bluffness (a) relationship between H_R and α, β (b) relationship between H_S and α, β.

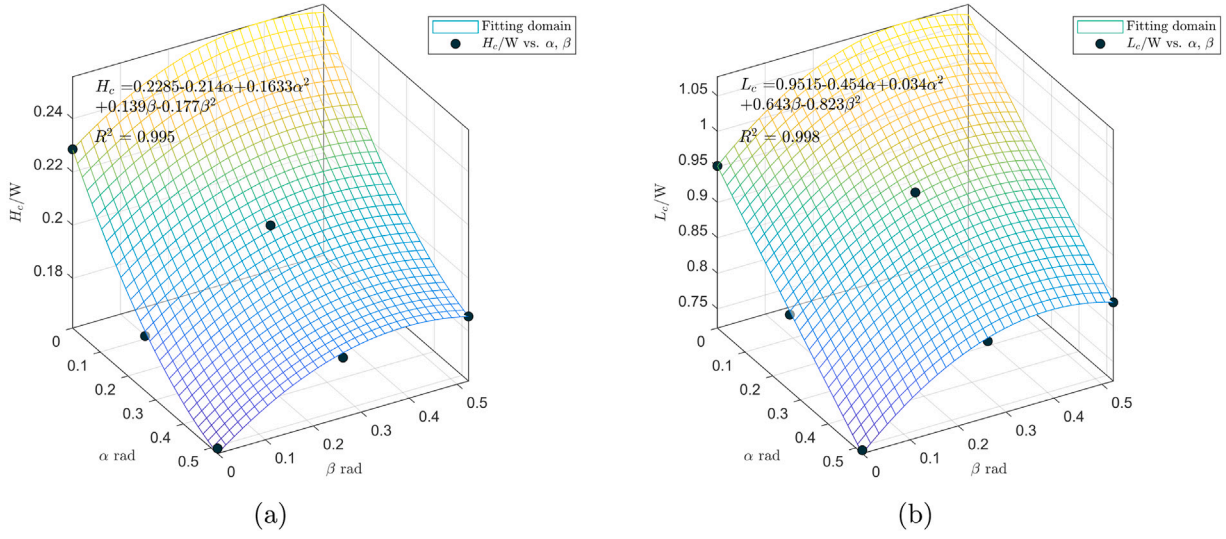

Fig. 26. Fitting domain for the height and length of the centre of the separation bubble and bluffness (a) relationship between H_c and α, β (b) relationship between L_c and α, β.

Fig. 27. The Class 70 validation case locomotive. (a) Class 70 locomotive (b) the CFD mesh and key dimensions, given here in the reduced 1/25th scale in m.

4. Conclusion

In this paper, the simulation of a freight train entering into a tunnel is carried out to visualise the flow separation around the blunted train nose. The results obtained from the simulations are adopted to calculate the input parameters for a novel redeveloped 1D numerical model, which, for the first time, is capable of considering freight train geometries. In addition, a parameterisation study for the size of the separation bubble is undertaken based on a simplified generic locomotive geometry. This numerical approach is then further validated

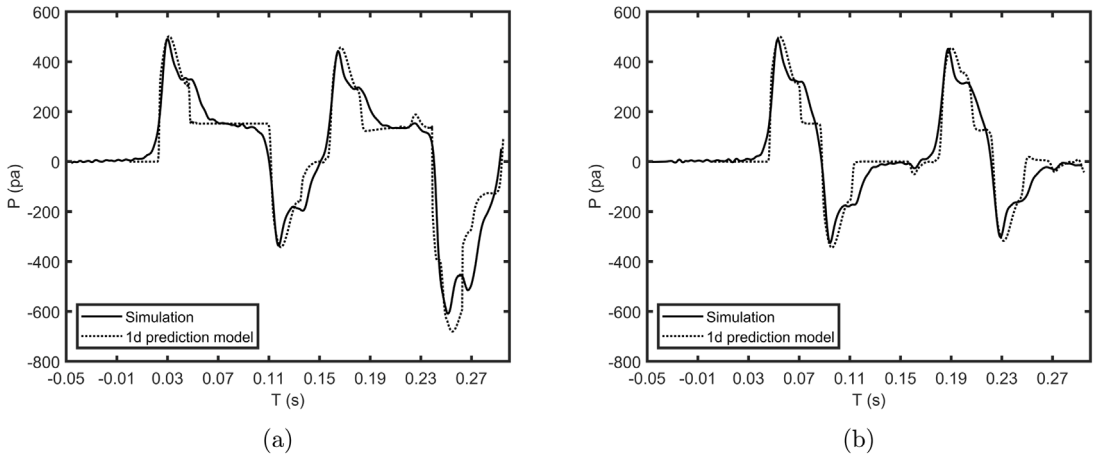

Fig. 28. Comparison of pressure time history curves for a Class 70 locomotive passing through a tunnel obtained from the 1D prediction model and CFD simulation for measuring positions (a) 8 m from the tunnel entry portal and (b) 16 m from the tunnel entry portal.

for the Class 70 locomotive, which has a very different nose shape, with results indicating the successful ability of the 1D modelling approach. A series of important conclusions can be drawn as below:

(a) As a freight train enters into a tunnel, the separation bubble induced by the blunted head of the freight train will increase the effective blockage ratio. This will influence the initial pressure rise and the subsequent pressure changes as the pressure wave propagates inside tunnel.

(b) A redeveloped 1D model is built by modifying the boundary conditions at the train nose and adding an additional term to describe the effective area change due to the flow separation in the continuity equation. Furthermore, a separation bubble model is built to calculate the effective blockage area by dividing the head of the freight train to roof, windshield and coupling regions, and considering the separation bubble height for each region. The development of pressure waves calculated using the separation bubble model before and after modification of the 1D methodology is compared with experimental results in previous work. Results indicate that the traditional code failed to predict the maximum initial pressure rise. This issue is greatly improved after considering the influence of the separation bubble, reducing the error of the maximum pressure rise from 43% to 4%.

(c) The length and width of the vortex size on the top, corner, and side of the locomotive head are measured. The results indicate that increasing the leading edge angle can efficiently decrease the height and width of the separation bubble both at top and side of the train. When α increases from 0° to 30°, L_{R1}/L_{S1} decrease from $2.0W/1.78W$ to around $1.7W/1.3W$ and H_{R1}/H_{S1} decreases from $0.406W/0.429W$ to around $0.28W/0.196W$ respectively.

(d) Increasing the sub-angle between the windshield and the roof edge causes the source node, where the separation length is the shortest on the side of the train surface, to tend to move from the top corner to the middle height of the train. However, the sub-angle has only a minor influence on the separation bubble on the roof.

(e) To further improve the 1D model robustness to apply to various types of freight trains, a parameterisation study is undertaken to get the fitting equation of the relationship between the parameters proposed in the separation bubble model (the height of the separation bubble in different regions) and bluntness of the train head. The accuracy and applicability of the parameterisation equation and the separation bubble model illustrates good agreement with CFD techniques when tested against the Class 70 locomotive shape, suggesting the novel 1D methodology is well validated.

The important outputs from this research have provided a valuable tool and information for academia and industry in relation to tunnel and freight train design and operation.

CRediT authorship contribution statement

Zhen Liu: Methodology, Software, Formal analysis, Investigation, Writing – original draft. **David Soper:** Conceptualization, Supervision, Writing – review & editing. **Hassan Hemida:** Supervision, Resources. **Boyang Chen:** Visualization, Writing – review & editing.

Declaration of competing interest

The authors declare that they have no known competing financial interests or personal relationships that could have appeared to influence the work reported in this paper.

Data availability

Data will be made available on request.

Appendix

MOC method

The mathematical method to solve the set of quasilinear hyperbolic partial differential equations is the MOC (method of characteristics). Firstly, these equations are non-dimensionalised by reference quantities (the reference speed of sound and the reference length). These are then replaced with pseudo-Riemann variables λ, β and a function of the entropy of the gas A_A. The Riemann variables are defined from Eqs. (19) to (21),

$$\lambda = \frac{a}{a_R} + \frac{\kappa-1}{2}\frac{u}{a_R} = A + \frac{\kappa-1}{2}U \tag{19}$$

$$\beta = \frac{a}{a_R} - \frac{\kappa-1}{2}\frac{u}{a_R} = A - \frac{\kappa-1}{2}U \tag{20}$$

$$A_A = \frac{a_A}{a_R} \tag{21}$$

This obtains the characteristic equations which involve the direction conditions for these three families of characteristic curves and the corresponding compatibility equations. The direction conditions and

the calculation of corresponding compatibility conditions of the disturbance characteristics (λ and β) are given in Eqs. (22) and (23).

$$\left(\frac{\mathrm{d}X}{\mathrm{d}Z}\right)_{\substack{\lambda\\ \beta}} = U \pm A \tag{22}$$

$$\begin{aligned} d_\beta^\lambda &= \Delta_{\beta_{A_A}}^\lambda + \Delta_{\beta_E}^\lambda + \Delta_{\beta_f}^\lambda + \Delta_{\beta_h}^\lambda = \frac{\lambda+\beta}{2}\frac{d_A}{A_A} - \frac{(\lambda+\beta)(\lambda-\beta)}{4E}\frac{\mathrm{d}E}{\mathrm{d}X}\,\mathrm{d}Z \\ &\mp \frac{\kappa-1}{2}\left[1 \mp 2\frac{(\lambda-\beta)}{(\lambda+\beta)}\right]\frac{l_R}{a_R^2}q\mathrm{d}Z + \frac{(\kappa-1)^2}{(\lambda+\beta)}\frac{(q-w)}{a_R^3}l_R dZ \end{aligned} \tag{23}$$

in which $\Delta_{\beta_{A_A}}^\lambda$, $\Delta_{\beta_E}^\lambda$, $\Delta_{\beta_f}^\lambda$, $\Delta_{\beta_h}^\lambda$ refers to the change on disturbance characteristics influenced by entropy, cross-sectional area, frictional effect and heat transfer. Similarly, the direction condition and the equation to calculate compatibility condition for path line characteristic A_A are given as follows,

$$\left(\frac{dX}{dZ}\right)_{A_A} = U \tag{24}$$

$$\begin{aligned} dA_A &= \Delta A_{Af} + \Delta A_{Ah} \\ &= 2\frac{(\lambda-\beta)}{(\lambda+\beta)^2}\frac{1}{a_R^2}q\,dZ + \frac{2(\kappa-1)}{(\lambda+\beta)^2}\frac{(q-w)}{a_R^3}l_R dZ \end{aligned} \tag{25}$$

Note that the uppercase letter in each of these equations refers to non-dimensionalised variables. When the Riemann variables at the moment Z are known, the discrete Reimann variables can be calculated through the Eqs. (23) and (25). Thus the variables at the next time step $Z + \Delta Z$ can be deduced by interpolation using a reversed mesh method. Readers may find a more detailed overview on solving the characteristic variables using the MOC method in Woods and Pope (1981).

References

Benchikh Le Hocine, A.E., Lacey, R.J., Poncet, S., 2019. Turbulent flow over a D-section bluff body: a numerical benchmark. Environ. Fluid Mech. 19 (2), 435–456.

Chen, G., Li, X.-B., Liu, Z., Zhou, D., Wang, Z., Liang, X.-F., Krajnovic, S., 2019. Dynamic analysis of the effect of nose length on train aerodynamic performance. J. Wind Eng. Ind. Aerodyn. 184, 198–208.

Chen, Y.J., Shao, C.P., 2013. Suppression of vortex shedding from a rectangular cylinder at low Reynolds numbers. J. Fluids Struct. 43, 15–27.

Cross, D., Hughes, B., Ingham, D., Ma, L., 2015. A validated numerical investigation of the effects of high blockage ratio and train and tunnel length upon underground railway aerodynamics. J. Wind Eng. Ind. Aerodyn. 146, 195–206.

DfT, 2007. Delivering a sustainable railway. In: Technical report, Vol. 1. Department for Transport..

Flynn, D., Hemida, H., Soper, D., Baker, C., 2014. Detached-eddy simulation of the slipstream of an operational freight train. J. Wind Eng. Ind. Aerodyn. 132, 1–12.

Fox, J., Henson, D., 1971. The prediction of the magnitudes of pressure transients generated by a train entering a single tunnel. Proc. Inst. Civ. Eng. 49 (1), 53–69.

Gao, Y., Chow, W.K., 2005. Numerical studies on air flow around a cube. J. Wind Eng. Ind. Aerodyn. 93 (2), 115–135.

Giappino, S., Melzi, S., Tomasini, G., 2018. High-speed freight trains for intermodal transportation: Wind tunnel study on the aerodynamic coefficients of container wagons. J. Wind Eng. Ind. Aerodyn. 175, 111–119.

Hellsten, A., Laine, S., Hellsten, A., Laine, S., 1997. Extension of the k-omega-SST turbulence model for flows over rough surfaces. In: 22nd Atmospheric Flight Mechanics Conference. p. 3577.

Hemida, H., Baker, C., 2010. Large-eddy simulation of the flow around a freight wagon subjected to a crosswind. Comput. & Fluids 39 (10), 1944–1956.

Howe, M., Iida, M., Fukuda, T., 2003. Influence of an unvented tunnel entrance hood on the compression wave generated by a high-speed train. J. Fluids Struct. 17 (6), 833–853.

Huo, X., Liu, T., Chen, Z., Li, W., Gao, H., 2022. Effect of the formation type with different freight vehicles on the train aerodynamic performance. Veh. Syst. Dyn. 60 (11), 3868–3896.

Iliadis, P., Soper, D., Baker, C., Hemida, H., 2019. Experimental investigation of the aerodynamics of a freight train passing through a tunnel using a moving model. Proc. Inst. Mech. Eng. F 233 (8), 857–868.

Ji, P., Wang, T.-t., Wu, F., 2019. Calculation grid and turbulence model for numerical simulating pressure fluctuations in high-speed train tunnel. J. Central South Univ. 26 (10), 2870–2877.

Kalitzin, G., Medic, G., Xia, G., 2016. Improvements to SST turbulence model for free shear layers, turbulent separation and stagnation point anomaly. In: 54th AIAA Aerospace Sciences Meeting. p. 1601.

Kedare, S.B., Sharma, S.C., Harsha, S.P., 2015. Computational fluid dynamics analysis of empty railway freight wagons. Int. J. Veh. Struct. Syst. 7 (1), 25.

Keogh, J., Barber, T., Diasinos, S., Doig, G., 2016. The aerodynamic effects on a cornering ahmed body. J. Wind Eng. Ind. Aerodyn. 154, 34–46.

Khayrullina, A., Blocken, B., Janssen, W., Straathof, J., 2015. CFD simulation of train aerodynamics: train-induced wind conditions at an underground railroad passenger platform. J. Wind Eng. Ind. Aerodyn. 139, 100–110.

Kocoń, A., Flaga, A., 2021. Critical velocity measurements of freight railway vehicles roll-over in wind tunnel tests as the method to assess their safety at strong cross winds. J. Wind Eng. Ind. Aerodyn. 211, 104559.

Krajnović, S., 2009. Large eddy simulation of flows around ground vehicles and other bluff bodies. Phil. Trans. R. Soc. A 367 (1899), 2917–2930.

Krajnovic, S., Davidson, L., 2002. Large-eddy simulation of the flow around a bluff body. AIAA J. 40 (5), 927–936.

Krajnović, S., Davidson, L., 2005a. Flow around a simplified car, part 1: large eddy simulation.

Krajnović, S., Davidson, L., 2005b. Flow around a simplified car, part 2: understanding the flow.

Li, C., Burton, D., Kost, M., Sheridan, J., Thompson, M.C., 2017. Flow topology of a container train wagon subjected to varying local loading configurations. J. Wind Eng. Ind. Aerodyn. 169, 12–29.

Li, X.-h., Deng, J., Chen, D.-w., Xie, F.-f., Zheng, Y., 2011. Unsteady simulation for a high-speed train entering a tunnel. J. Zhejiang Univ.-Sci. A 12 (12), 957–963.

Li, C., Kost, M., Burton, D., Sheridan, J., Thompson, M.C., 2015. Wind tunnel investigation of a double stacked wagon in free-stream. In: Fluids Engineering Division Summer Meeting, Vol. 57212. American Society of Mechanical Engineers, V001T16A002.

Liang, G., Liu, T., Xia, Y., Chen, Z., Dong, X., Chen, X., 2023. Application of periodic boundaries in freight train aerodynamic performance simulations. Alex. Eng. J. 70, 315–329.

Lim, H.C., Thomas, T., Castro, I.P., 2009. Flow around a cube in a turbulent boundary layer: LES and experiment. J. Wind Eng. Ind. Aerodyn. 97 (2), 96–109.

Liu, Z., Chen, G., Zhou, D., Wang, Z., Guo, Z., 2021. Numerical investigation of the pressure and friction resistance of a high-speed subway train based on an overset mesh method. Proc. Inst. Mech. Eng. F 235 (5), 598–615.

Liu, T.-h., Tian, H.-q., Liang, X.-f., 2010. Aerodynamic effects caused by trains entering tunnels. J. Transp. Eng. 136 (9), 846–853.

Liu, Z., Yu, Z., Chen, X., Cao, R., Zhu, F., 2020. An investigation on external airflow around low-rise building with various roof types: PIV measurements and LES simulations. Build. Environ. 169, 106583.

Lunghi, G., Pasqualetto, E., Rocchio, B., Mariotti, A., Salvetti, M.V., 2022. Impact of the lateral mean recirculation characteristics on the near-wake and bulk quantities of the BARC configuration. Wind Struct. 34 (1), 115–125.

Maleki, S., Burton, D., Thompson, M.C., 2017. Assessment of various turbulence models (ELES, SAS, URANS and RANS) for predicting the aerodynamics of freight train container wagons. J. Wind Eng. Ind. Aerodyn. 170, 68–80.

Maleki, S., Burton, D., Thompson, M.C., 2019. Flow structure between freight train containers with implications for aerodynamic drag. J. Wind Eng. Ind. Aerodyn. 188, 194–206.

Mei, Y., 2013. A generalized numerical simulation method for pressure waves generated by high-speed trains passing through tunnels. Adv. Struct. Eng. 16 (8), 1427–1436.

Munoz-Paniagua, J., García, J., Crespo, A., 2014. Genetically aerodynamic optimization of the nose shape of a high-speed train entering a tunnel. J. Wind Eng. Ind. Aerodyn. 130, 48–61.

Ogawa, T., Fujii, K., 1997. Numerical investigation of three-dimensional compressible flows induced by a train moving into a tunnel. Comput. & Fluids 26 (6), 565–585.

Östh, J., Krajnović, S., 2014. A study of the aerodynamics of a generic container freight wagon using large-eddy simulation. J. Fluids Struct. 44, 31–51.

Paik, J., Sotiropoulos, F., Porté-Agel, F., 2009. Detached eddy simulation of flow around two wall-mounted cubes in tandem. Int. J. Heat Fluid Flow 30 (2), 286–305.

Perry, A.E., Chong, M.S., 1987. A description of eddying motions and flow patterns using critical-point concepts. Annu. Rev. Fluid Mech. 19 (1), 125–155.

Premoli, A., Rocchi, D., Schito, P., Tomasini, G., 2016. Comparison between steady and moving railway vehicles subjected to crosswind by CFD analysis. J. Wind Eng. Ind. Aerodyn. 156, 29–40.

Raghunathan, R.S., Kim, H.-D., Setoguchi, T., 2002. Aerodynamics of high-speed railway train. Prog. Aerosp. Sci. 38 (6–7), 469–514.

Richards, P., Norris, S., 2015. LES modelling of unsteady flow around the silsoe cube. J. Wind Eng. Ind. Aerodyn. 144, 70–78.

Rocchio, B., Mariotti, A., Salvetti, M., 2020. Flow around a 5: 1 rectangular cylinder: Effects of upstream-edge rounding. J. Wind Eng. Ind. Aerodyn. 204, 104237.

Soper, D., 2016. The Aerodynamics of a Container Freight Train. Springer.

Soper, D., Baker, C., Sterling, M., 2014. Experimental investigation of the slipstream development around a container freight train using a moving model facility. J. Wind Eng. Ind. Aerodyn. 135, 105–117.

Taylor, Z.J., Palombi, E., Gurka, R., Kopp, G.A., 2011. Features of the turbulent flow around symmetric elongated bluff bodies. J. Fluids Struct. 27 (2), 250–265.

Vardy, A.E., 1976. On the use of the method of characteristics for the solution of unsteady flows in networks. In: Proceedings of the 2nd International Conference on Pressure Surges, BHRA Fluid Engineering, London, Vol. 2. pp. 15–30.

Vardy, A., Reinke, P., 1999. Estimation of train resistance coefficients in tunnels from measurements during routine operation. Proc. Inst. Mech. Eng. F 213 (2), 71–87.

William-Louis, M.-P., Gregoire, R., 2002. 1-d calculations of pressure fluctuations outside and inside a pressure sealed high-speed trainset travelling through tunnels. In: TRANSAERO—a European Initiative on Transient Aerodynamics for Railway System Optimisation. Springer, pp. 342–357.

Woods, W., Gawthorpe, R., 1972. The train and tunnel-a large scale unsteady flow machine. In: 2nd International JSME Symposium on Fluid Machinery and Fluidic. pp. 249–258.

Woods, W., Pope, C., 1981. A generalised flow prediction method for the unsteady flow generated by a train in a single-track tunnel. J. Wind Eng. Ind. Aerodyn. 7 (3), 331–360.

Xia, Y., Liu, T., Gu, H., Guo, Z., Chen, Z., Li, W., Li, L., 2020. Aerodynamic effects of the gap spacing between adjacent vehicles on wind tunnel train models. Eng. Appl. Comput. Fluid Mech. 14 (1), 835–852.